Sensitivity of Arctic sea ice to melt pond processes and atmospheric forcing: A model study

Jean Sterlin, Thierry Fichefet, François Massonnet, Olivier Lecomte, Martin Vancoppenolle

Ocean Modelling 167 (2021) 101872

Contents lists available at ScienceDirect

Ocean Modelling

journal homepage: www.elsevier.com/locate/ocemod

Sensitivity of Arctic sea ice to melt pond processes and atmospheric forcing: A model study

Jean Sterlin [a,*], Thierry Fichefet [a], François Massonnet [a], Olivier Lecomte [a], Martin Vancoppenolle [b]

[a] Georges Lemaître Centre for Earth and Climate Research, Earth and Life Institute, Université catholique de Louvain, Louvain-la-Neuve, Belgium
[b] Laboratoire d'Océanographie et du Climat (LOCEAN-IPSL), Centre National de la Recherche Scientifique (CNRS), Sorbonne Universités (UPMC, Univ Paris 06), 4 Place Jussieu, F-75005 Paris, France

ARTICLE INFO

Keywords:
Melt ponds
Atmospheric reanalysis and forcing
Sea ice model
Ocean general circulation model
Arctic climate
Albedo

ABSTRACT

Melt ponds are pools of meltwater forming principally on Arctic sea ice during the melt season. The albedo of melt ponds is a key component of the surface energy balance. For this reason, various melt pond schemes have been developed for climate models. These schemes require assumptions on the physical processes governing melt ponds as well as a knowledge of the atmospheric state, which are not perfectly known. In this study, we investigate the effects of the sources of uncertainty from the prescribed atmospheric surface state, the melt pond scheme definition and the refreezing formulation of melt ponds on the simulated Arctic sea ice and melt pond properties with the NEMO-LIM3 ocean–sea ice general circulation model. We find that the simulated melt pond state is largely controlled by the freezing point of melt ponds. The representation of melt ponds is in better agreement with observations when using the freezing point of −0.15 °C compared to the value of −2.00 °C, in our model set-up. All the simulations feature positive trends in melt pond area fraction over the past decades. However, only 3 out of 8 simulations have significant positive trends in melt pond volume per sea ice area. This suggests an influence of the sea ice state for melt ponds over the last 30 years. Overall, we find that the simulated sea ice state, and in particular sea ice volume, is more affected by changes in the prescribed atmospheric forcing than by changes in the prescribed melt pond scheme or refreezing formulation. Including explicit melt pond schemes in large-scale sea-ice models offer the possibility to improve the representation of the surface energy balance in climate general circulation models. Our results underline that, in parallel to these efforts in model developments, improved estimates of surface atmospheric conditions will be required to achieve more realistic sea ice states.

1. Introduction

Arctic sea ice is changing. Since the beginning of sea ice observations from satellites in the seventies, the Arctic sea ice extent has declined all year round, with a maximum decrease in September at the end of the melt season (Serreze and Meier, 2018). The mean sea ice thickness in the Arctic is decreasing in both winter and summer seasons (Kwok and Rothrock, 2009). In addition, sea ice is becoming younger, with a more rapid reduction of the area covered by multi-year ice (MYI) than first-year ice (FYI) (Maslanik et al., 2011). Among these changes, the decrease in the mean surface albedo in the Arctic sea ice zone (Riihelä et al., 2013) is of importance for the Arctic climate because of the ice-albedo feedback (Curry et al., 1995), which tends to amplify any temperature changes in polar regions.

Melt ponds are pools of meltwater forming on sea ice during the summer months. Melt ponds are an important aspect of the surface energy balance over sea ice. The albedo of melt ponds is lower than the surrounding ice and snow areas (Shine and Henderson-Sellers, 1985; Grenfell, 2004). Additionally, the transmission of sunlight is larger in ponded ice regions (Frey et al., 2011), supplying heat to the ocean surface layer and further enhancing basal ice melt. The transmitted light can also sustain primary production under the ice (Arrigo et al., 2012). Furthermore, melt ponds alter the ice–atmosphere fluxes of momentum and heat, as melt pond edges influence the mean surface roughness of the ice surface (Lüpkes et al., 2013; Tsamados et al., 2014). Lastly, melt ponds act as buffer reservoirs of meltwater on the ice surface. They either delay the input of freshwater to the ocean during the melt season, or they redirect the meltwater to the sea ice system when melt ponds refreeze. The refreezing of melt ponds leads to latent heat release that limits basal ice growth (Flocco et al., 2015).

The amount of water in the ponds is controlled by the net flux of freshwater. The input of freshwater takes its source from the melting

* Corresponding author.
E-mail address: jean.sterlin@uclouvain.be (J. Sterlin).

https://doi.org/10.1016/j.ocemod.2021.101872
Received 30 January 2021; Received in revised form 31 May 2021; Accepted 20 August 2021
Available online 2 September 2021

of the snow and ice layers at the surface and liquid precipitation falling onto the ice cover. Freshwater losses occur through a variety of processes: lateral transport to floe edges and leads in the vicinity of the ponds, vertical seepage due to the porous nature of sea ice and the presence of cracks (Freitag and Eicken, 2003; Scott and Feltham, 2010), water losses by mechanical processes such as ridging and rafting and refreezing of the ponds during cold air events (Flocco et al., 2015). Ultimately, melt ponds disappear when the ice is too thin to support them or when the volume of meltwater they contain become null. In autumn, melt ponds refreeze by forming an ice-lid at their upper surface. The ice-lid prevents exchanges with the atmosphere and may further delay the refreezing of melt ponds to over a month (Flocco et al., 2015). The surface topography and the ice permeability control the spatial distribution of the melt ponds (Eicken, 2002). On deformed MYI, melt ponds are generally deeper and cover smaller areas (about 30 % of the ice area), whereas ponds on FYI are shallower and extend between 40 to 50 % (Fetterer and Untersteiner, 1998), up to 90 % on flat ice (Perovich et al., 2011).

Because of their importance, melt pond schemes of different levels of complexity have been developed and introduced in large-scale sea ice models used in general circulation models. These schemes can be classified into two groups. The first group assumes a fixed relationship between the area fraction and the pond depth. Holland et al. (2012) use a linear fit of observations collected during the Surface Heat Budget of the Arctic Ocean (SHEBA) campaign to estimate the proportionality constant between the melt pond area and depth. Zhang et al. (2018) modified the SHEBA linear fit to increase the pond depth over thicker ice in order to reproduce the observed pond characteristics. Pedersen et al. (2009) derived a scheme with an aspect ratio relation obtained from the results of a mathematical model (Lüthje et al., 2006). The second group of schemes avoid the use of an explicit formulation of the aspect ratio but relies on theoretical considerations to define the melt pond geometry. The level-ice melt ponds scheme of Hunke et al. (2013) carries the volume and area fractions of melt ponds as tracers on the level ice area. The underlying idea of the level-ice melt pond scheme is that meltwater collects preferably on level ice. Flocco and Feltham (2007) developed another approach using the distribution of the ice thickness to deduce the surface height distribution of the ice. In the scheme, meltwater accumulates on ice categories with the smallest height first and gradually expands over higher ice surface categories. The scheme was further refined and adapted to the Los Alamos CICE sea ice model (Flocco et al., 2010, 2012).

Despite our understanding of melt pond processes, current melt pond schemes developed for large-scale sea ice models result in contradictory trends in melt pond areas over the past decades. Schröder et al. (2014) obtained a positive trend in melt pond area fraction of sea ice using the scheme of Flocco et al. (2012), whereas Zhang et al. (2018) found a weak negative but non-significant trend in melt pond volume and area over the same period with an explicit aspect ratio based scheme.

Apart from the conceptual difference in the definition of the aspect ratio, the two studies differ in the determination of the conditions leading to the refreezing of melt ponds. Zhang et al. (2018) use the formulation of Holland et al. (2012), while Flocco et al. (2012) use a more complex ice-lid formulation. Lastly, the atmospheric surface state has an impact on the melting rate of the snow and ice at the surface and thus on the meltwater available for ponds. Uncertainties in the atmospheric datasets may propagate to the simulated melt pond area and volume.

In this paper, we aim to: (1) evaluate the effect of the conceptual differences of aspect ratio definitions in melt pond schemes for the representation of melt ponds; (2) elucidate the role that refreezing processes can have on the seasonal evolution of Arctic sea ice melt ponds; (3) estimate how uncertainties in atmospheric reanalyses affect the simulated results. We address the three questions above both for the simulated melt pond and large-scale sea ice properties over the period for which observations are available (1980–2015) in the Northern Hemisphere.

In Section 2, we describe the configuration of the ocean–sea ice model NEMO–LIM used in this study, together with the atmospheric forcing datasets, the melt pond schemes and the formulation of the refreezing of melt ponds. Then, in Section 3, we present and discuss the results derived from the set of simulations carried out with the model. Concluding remarks are finally given in Section 4.

2. Methods

2.1. Numerical models

In this study, we use the Océan PArallélisé (OPA) ocean model coupled to the ice model LIM within the framework of NEMO (Nucleus for European Modelling of the Ocean) version 3.6 stable (SVN revision 7619). OPA is a finite-difference, hydrostatic, primitive-equation model (Madec et al., 2017). The sea ice model is LIM version 3 (Vancoppenolle et al., 2009; Rousset et al., 2015). LIM features a discrete subgrid-scale ice thickness distribution (ITD) (Thorndike et al., 1975) with five ice categories. The boundaries of the thickness categories are 0, 0.45, 1.13, 2.14, 3.67 and 99 m (Massonnet et al., 2019, see Eq. (2)). The salinity, age and enthalpy of the ice are defined separately for each category. We adopt the vertical thermodynamic formulation of Bitz and Lipscomb (1999) and Vancoppenolle et al. (2007) with five layers of ice and one of snow, for each ice categories. The ice dynamics are represented by the elastic–viscous–plastic (EVP) formalism (Hunke et al., 2019) adapted to the Arakawa C grid (Bouillon et al., 2009). The advection of sea ice properties is computed with the second-order scheme of Prather (1986) for each of the categories of the ITD.

2.2. Atmospheric datasets and surface forcing method

In our configuration, the surface boundary conditions of NEMO-LIM are computed following the formulation of the Coordinated ocean–ice Reference Experiments (CORE) of NEMO–LIM. CORE requires as surface inputs the wind speed components, the air temperature and specific humidity, the short and longwave downward radiation, and the snow and liquid precipitation rates. From these surface variables, the wind stress, sensible and latent turbulent heat fluxes are estimated through bulk formulas. Transfer coefficients over the ocean for momentum, sensible and latent heat fluxes are calculated according to Large and Yeager (2004, 2008) using the Monin–Obukhov similarity theory. The transfer coefficients between the atmosphere–ice interface are set equal to 1.4×10^{-3}. The net surface longwave radiation flux is given from the difference of the downwelling longwave radiation with the upward black body radiation flux, with the emissivity set to 0.95 over the ice. The shortwave radiation absorbed at the surface is calculated using the ice-albedo scheme of Shine and Henderson-Sellers (1985), assuming a constant cloud fraction of 0.81. The ocean albedo is set equal to 0.066 (e.g. Pegau and Paulson (2001)). The evaporation of seawater and sublimation at the surface of the ice cover are calculated from the latent surface heat fluxes. The solid precipitation is prescribed by the atmospheric dataset, dismissing the need for a scheme such as the one of Ledley (1985). The amount of snow is redistributed between the ocean and ice as a function of the open water area, to account for the effect of the blowing snow (Lecomte et al., 2015). Liquid precipitation falling on the ice is collected in the ocean.

The first atmospheric dataset we use is the DRAKKAR forcing set (DFS), version 5.2 from the DRAKKAR modelling community (Brodeau et al., 2010; Dussin et al., 2016). This dataset is based on ERA40 (Uppala et al., 2005) and ERA-interim (Dee et al., 2011) reanalyses. DFS covers the period 1958 to 2015, with a resolution of 80 km. The frequency is daily for precipitation and radiation fluxes, and 3-hourly for the wind speed components, the surface air temperature (SAT) and surface air specific humidity. An assessment of the ERA-interim

variables by Dussin et al. (2016) led to the introduction of the following corrections: increasing of the wind speed in the intertropical band, adjustments of the radiations to equilibrate the global heat balance, removal of time discontinuities in the liquid precipitation fields, and reduction of the SAT and specific humidity in the Arctic and the Southern Ocean, near the Antarctic continent (Dussin et al., 2016). DFS relies on the ERA40 anomalies in wind speeds, SAT and humidity, between 1958 and 1978. These anomalies are added to a daily climatology of the modified ERA-interim dataset.

The second atmospheric forcing dataset chosen is the Japanese 55-year reanalysis, hereafter referred to as JRA. This product is a global atmospheric reanalysis (Kobayashi et al., 2015) being conducted by the Japan Meteorological Agency (JMA) and the Central Institute of Electric Power Industry (CRIEPI). It spans from 1958 to present times. The frequency is 3 h and the spatial resolution is 60 km. The reanalysis is based on the 25 years Japanese reanalysis (JRA-25), with the addition of a four-dimensional variational analysis (4D-Var), a variation bias correction (VarBC) for satellite radiances and smoother transitions between the observational datasets. The quality of JRA over DFS lies with the use of the same methodology over the entire period covered by the dataset.

2.3. Implementation of the melt pond schemes in the sea ice model

The melt ponds are carried as tracers of volume v_{ip} and area fraction a_{ip} on the ice surface of each thickness category. The geometrical properties of the ponds are defined in the melt pond schemes according to the formulation of the aspect ratio, as described in the following sections.

The amount of meltwater added to the melt ponds is derived from the volume changes due to the melting of the snow and the ice surface layers, between each time step. A fraction of the total surface meltwater becomes available for ponding; the remaining fraction runs off the ice and is lost to the ocean. The fraction r is given by Eq. (1):

$$r(a_i) = 0.15 + 0.55a_i \tag{1}$$

as a function of the ice concentration per category a_i. We follow the formulation of Icepack sea ice column physics (Hunke et al., 2019) from CICE consortium to specify the fraction. A single ice category receives at most 70 % of the available surface meltwater and at least 15 %. This formulation differs slightly from Holland et al. (2012) and Flocco et al. (2012). The use of a_i reflects better the allocation of meltwater among the ice categories in case of asymmetries in the ice thickness distribution. The liquid precipitation is not included in the ice model. Instead, CORE sends the water flux directly to the ocean. This assumption is reasonable as snowfall is presently the dominant form of precipitation in the Arctic (Bintanja and Andry, 2017).

2.4. Explicit aspect ratio melt pond scheme

As for the melt pond scheme with an explicit formulation of the aspect ratio, we follow closely the implementation of the melt pond scheme of Holland et al. (2012) in the community earth system model (CESM). We will refer to this scheme as CESM. The aspect ratio relation is given by $a_{ip}/a_i = 0.8h_{ip}$. The relation is used to calculate the area fraction a_{ip} and depth h_{ip} of the ponds from v_{ip}. The relation was estimated by a linear fit of observations collected during SHEBA (Perovich, 2003). To bound the pond characteristics to physical ranges, the melt pond quantities undergo additional constraints. The pond depth cannot exceed 90 % of the ice thickness category. The ponds are cleared if the ice thickness is less than 0.10 m. Lastly, the meltwater removed from the ponds is transferred to the ocean.

2.5. Implicit aspect ratio melt pond scheme

In the second group of melt pond scheme, the melt ponds are defined without specifying explicitly the aspect ratio. We use the so-called topographic scheme (Flocco and Feltham, 2007; Flocco et al., 2010) in LIM (Lecomte et al., 2015). The version chosen here follows the one of Icepack, version 1.1.1, as documented by Hunke et al. (2019). This scheme is not able to resolve explicitly the surface morphology of the ice. Instead, the ice thickness distribution is separated into a distribution of the ice surface height and a distribution of the ice basal depth. To express the distribution of the surface height, the ice thickness categories are assumed to be in hydrostatic equilibrium and the ice in a grid cell to be rigid. The volume of meltwater available for ponding is then distributed over the surface height categories, filling up the categories from low to high surface height categories and considering saturated snow.

The topographic scheme features an additional sink of meltwater due to the porosity of the ice. The vertical seepage is calculated from the ice permeability using Darcy's law. The permeability is a cubic function of the fraction of brine (Golden et al., 2007). The greater the fraction of brine, the more porous the ice and the greater the permeability. The solid fraction of ice is given from mushy layer equations (Feltham et al., 2006), with salt concentrations in brine evaluated from polynomial functions of the internal ice temperature (Assur, 1958; Notz, 2005). The concentration of salt in ice crystals is set to 0.

2.6. Formulation of the refreezing of melt ponds

As mentioned earlier, the refreezing of melt ponds is a complex process to represent (Flocco et al., 2015). The melt pond salinity has a direct effect on the freezing point of melt ponds. The freezing rates of melt ponds depend not only on the heat content of the ponds but also on the stratification of the water column in the ponds (Kim et al., 2018). The representation of the heat and salt contents of melt ponds in climate models and their effects on sea ice is still an open question.

As a first approach, Holland et al. (2012) defined the refreezing of melt ponds empirically using the following expression:

$$V_{pnd}^{t+1} = V_{pnd}^{t} \exp\left(-0.01 \frac{T_{sfc} - T_{thr}}{T_{thr}}\right) \tag{2}$$

where t is the model time and $t + 1$ the time at the next iteration. The volume of meltwater is reduced by the exponential term of Eq. (2) when the ice surface temperature T_{sfc} is below the threshold T_{thr}. Holland et al. (2012) and Zhang et al. (2018) set T_{thr} to −2.0 °C, assuming the melting temperature for sea ice as 0 °C. The salinity of melt ponds may be important when melt ponds are connected to the ocean. Perovich et al. (2009) reported salinities of up to 29 ppt for such melt ponds, which correspond to a freezing point of −1.6 °C. Thus, the temperature threshold of −2.0 °C is arguably not realistic. However, the formulation of Holland et al. (2012) is designed to be a simple and effective method to refreeze melt ponds. Lastly, the mechanism is influenced by the model time step, where a reduction of the time step causes melt ponds to refreeze more rapidly.

As a second approach, Flocco et al. (2010) represented the refreezing of melt ponds by an ice-lid that develops on the pond surface when the surface temperature is below the freezing point of melt ponds. The thickness of the ice-lid is calculated using the Stefan energy budget law applied to the lid-pond interface, assuming a vertical linear temperature profile in the lid and a temperature in the ponds equals their freezing point. Melt ponds are assumed to have a non-zero salinity, and consequently a freezing point slightly below 0 °C. In version 1.1.1 of Icepack (Hunke et al., 2019), the freezing point of melt ponds is set to −0.15 °C. This temperature is the freezing point of water with a salinity of 2.6 PSU.

We have selected the refreezing formulation of Holland et al. (2012) to ensure the strict conservation of heat and mass in the model simply.

Table 1
Albedo values used in LIM for four different surface types, given for clear sky.

	Dry snow α_{snw}^{dry}	Melting snow α_{snw}^{mlt}	Dry ice α_{ice}^{dry}	Ponded ice α_{pnd}^{ref}	Open water α_{opw}
Albedo	0.80	0.65	0.72	0.25	0.066

The conservations of heat and mass help the integration of our work into Earth-System Models. The ice-lid formulation of Flocco et al. (2010) requires additional assumptions to redistribute heat and mass between the ice categories and the ocean. On the other hand, the amount of frozen water from Holland et al.'s (Holland et al., 2012) formulation is redirected to the ocean in the form of a salt flux, with no latent heat release. The treatment of freshwater flux in melt ponds and surface meltwater fluxes in LIM3 is identical.

The formulation of Holland et al. (2012) allows adjusting easily the freezing rates of melt ponds while keeping the dependence on the freezing point of melt ponds and the surface temperature. These enable us to examine the effects of two temperature thresholds. The threshold of −0.15 °C is associated to melt ponds with low salinity and high freezing rates, whereas −2.00 °C is linked to melt ponds with high salinity and low freezing rates.

2.7. Computation of the surface albedo

The albedo of the ice cover is calculated as the weighted mean of three different surface types: snow, bare ice and melt ponds. The first two types are determined following Shine and Henderson-Sellers (1985) with different sets of piecewise functions depending on the thicknesses of the ice or snow layers. The correction of Oberhuber (1988) is applied to adjust the weighted mean albedo over sea ice to overcast sky conditions. The melt pond surface type is specified by Eq. (3), as a function of the meltwater depth in the ponds (Lecomte et al., 2011):

$$\alpha_{pnd}\left(h_{pnd}\right) = \alpha_{pnd}^{ref} + (\alpha_{ice}^{dry} - \alpha_{pnd}^{ref}) \exp\left(-\frac{h_{pnd}}{\omega}\right) \tag{3}$$

where ω is the characteristic exponential length scale for pond albedo, set equal to 0.05 m (Lecomte et al., 2015). The albedo of ponded ice quickly converges towards the minimum reference melt pond albedo (α_{pnd}^{ref}) value of 0.25 as the water depth increases. A melt pond depth greater than 0.23 m results in more than 99 % of decrease in albedo over melt ponds. Ice surfaces with no pond or snow have the albedo of dry bare ice α_{ice}^{dry}. Reference albedo values are presented in Table 1.

2.8. Experimental design

Our experimental design consists of eight numerical simulations. We make use of the atmospheric forcing datasets DFS and JRA, along with the CORE forcing method, to define the boundary conditions at the ocean and ice surfaces. Furthermore, we combine the melt pond schemes of Holland et al. (2012) (CESM) and Flocco et al. (2010) (topographic) in association with the two atmospheric datasets. Lastly, we select the melt pond refreezing formulation of Holland et al. (2012) for both schemes and we test the temperatures −2.00 °C and −0.15 °C as the melt pond refreezing temperature thresholds.

The simulations extend from 1958 to 2015. We reduce the period of analysis to the last 30 years to allow a sufficient spin-up for the sea ice and ocean surface properties to stabilise. The ocean mesh is a 1° curvilinear tripolar grid of the ORCA family (Madec and Imbard, 1996). The grid cell edge length is ∼112 km at the equator, down to ∼46 km in the Arctic basin. The grid extends underneath the Antarctic ice shelves to allow the representation of ocean–ice shelf interactions, although such interactions are not explicitly represented in this study. There are 75 vertical levels in partial step z-coordinate. The vertical resolution increases from 200 m at the bottom to 1 m near the surface, following a double hyperbolic tangent function. The ocean model time step is 1 h with a call to the ice model every 6 h. The vertical mixing in the ocean is assured by a turbulent eddy kinetic energy scheme (Blanke and Delecluse, 1993). The horizontal Laplacian eddy viscosity is set to 20 000 $m^2 s^{-1}$, which is half the default value specified in NEMO–LIM.

As initial conditions, the ocean starts from rest, with the 3-D temperature and salinity fields prescribed by the World Ocean Atlas 2013 (WOA13) climatology (Locarnini et al., 2013; Zweng et al., 2013). The ocean is covered with sea ice when the sea surface temperature is less than 2 °C above the seawater freezing point. The initial characteristics of the ice are 3.0 m (1.0 m) ice thickness in the Northern (Southern) Hemisphere, 90 % ice concentration, −3.15 °C ice temperature, 6.3 g/kg ice salinity, 0.30 m snow depth. The river runoff consists of continental freshwater discharges (> 60 °S) and melting of icebergs in the Southern Ocean (< 60 °S), respectively given by Dai and Trenberth (2002) and Merino et al. (2016). In addition, ice shelf calving fluxes in the Antarctic are prescribed by Depoorter et al. (2013) and distributed at depth along the calving front. The sea surface salinity is restored towards the WOA13 climatology to avoid spurious model drifts. In ice-covered regions, this restoring is multiplied with the fraction of open water (one minus the ice concentration) to preserve ocean–ice interactions. The salinity relaxation time scale is equivalent to 300 days for a mixed layer depth of 50 m in ice-free regions.

The configuration of the model is closely related to those of Docquier et al. (2017), Barthélemy et al. (2017), Massonnet et al. (2019) among others. Our implementation of melt ponds in NEMO-LIM is based on the initial work of Lecomte et al. (2015), which may be used for comparison.

2.9. Observations

To assess the simulations, we make use of observational products to examine the model skill in representing the sea ice and melt ponds in the Arctic from 1980 to 2015. The products consist mainly of four large-scale datasets. Firstly, the sea ice concentrations generated by the NASA Team algorithm from Nimbus-7 SMMR and DMSP SSM/I-SSMIS passive microwave data (Cavalieri, 1996), hereafter referred to as NSIDC-0051, are used to evaluate the simulated sea ice concentrations and the ice extent and to estimate the errors in ice edge position. Secondly, we use the PIOMAS reanalysis for assessing the simulated Arctic sea ice volume, keeping in mind that this reanalysis is uncertain (Schweiger et al., 2011). Thirdly, the melt pond distributions on Arctic sea ice from Rösel et al. (2012) and Lee et al. (2020) are used to assess the representation of melt ponds. These two products are derived from the Moderate Resolution Imaging Spectroradiometer (MODIS). MODIS sensors operate in the visible and infrared part of the spectrum. Thus, measurements are influenced by the fraction of clouds in the atmosphere, altering the ability of the two algorithms to resolve the fractions of melt ponds and sea ice. We retrieved version 2 of the dataset of Rösel et al. (2012) from the Integrated Climate Data Center (ICDC, icdc.cen.uni-hamburg.de), University of Hamburg, Hamburg, Germany, October 2018. This dataset covers the years 2000 to 2011, at a spatial resolution of 12.5 km and a temporal resolution of 8 days. The dataset of Lee et al. (2020) was downloaded from the UK Polar Data Centre (UK PDC), hosted by the British Antarctic Survey. We select the years 2000 to 2015 of the 8-day average product from the repository. The spatial resolution of this product is 5 km.

3. Results and discussion

3.1. Simulation of melt ponds by NEMO–LIM

Fig. 1 shows the mean seasonal cycles of the melt pond (MP) area fraction of sea ice, hereafter referred to as the MP area fraction, as modelled by NEMO–LIM over 2000–2011. As a point of comparison, the equivalent mean seasonal cycles from the datasets of Rösel et al.

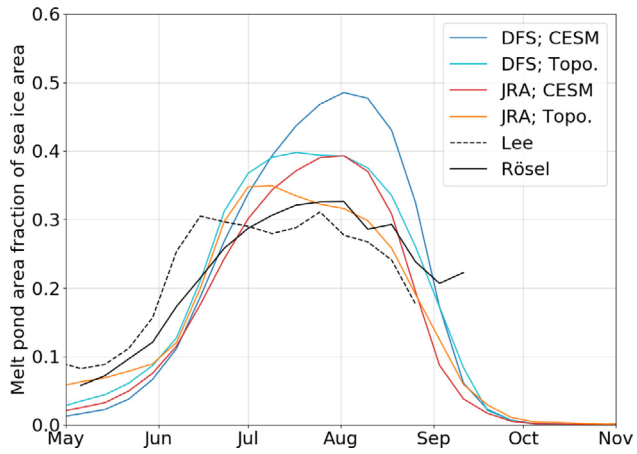

Fig. 1. Mean seasonal cycles of the melt pond area fraction of sea ice averaged between 2000 and 2011 in the Northern Hemisphere where the ice concentration is strictly positive. The group of simulations has T_{thr} set equal to −0.15 °C. The mean seasonal cycles derived from MODIS by Rösel et al. (2012) and Lee et al. (2020) are drawn in black.

(2012) and Lee et al. (2020) are shown in black in the same figure. The means of the MP area fractions are calculated on a weekly basis in the Northern Hemisphere and in the presence of sea ice (non-zero ice concentration). The means are weighted by the area of the grid cells. The group of simulations has T_{thr} set equal to −0.15 °C. The temperature of −0.15 °C corresponds to a scenario of melt ponds containing a small amount of salt and high refreezing rates of melt ponds.

The mean seasonal cycles of the simulated MP area fraction compare well with the datasets of Rösel et al. (2012) and Lee et al. (2020), especially the onsets and outsets of melt ponds. The simulated onset of the MP area fraction is slightly delayed by a couple of days compared to the dataset of Rösel et al. (2012) and by about one week compared to the one of Lee et al. (2020). In late August, the simulated MP area fraction starts to reduce similarly to the cycles derived from the MODIS based datasets.

NEMO–LIM simulates large MP area fractions in July and August. Other modelling studies using the ice-lid refreezing mechanism (Flocco et al., 2012; Schröder et al., 2014; Lecomte et al., 2015) show significantly smaller seasonal maxima in MP area fractions than those obtained from our simulations. These studies present principally the mean exposed MP area fractions. The multiplying factor between the exposed and total MP area fractions is between 1.75 and 2 (Flocco et al., 2012; Lecomte et al., 2015) in July. The exposed MP area fractions are closer in definition to the measurable MP area fractions from MODIS. Lastly, in the current configuration, NEMO–LIM tends to underestimate the ice concentration in summer and to simulate the minimum ice extent in advance by 2–3 weeks compared to observations (see Section 3.4). Normalising the melt pond area by the sea ice area leads to larger MP area fractions (of sea ice area).

The product of Rösel et al. (2012) features an increase in the mean MP area fraction in September, which is not observed in Lee et al.'s (Lee et al., 2020) dataset. This increase is due to uncertainties in the retrieval method of Tschudi et al. (2005, 2008) in late summer. This method tends to overestimate melt ponds on thin ice because of the spectral signatures of the surface types. The bias becomes important in the marginal ice zone or in September as the sea ice extent is minimum and melt ponds either refreeze or decay. By the end of September, the remaining melt ponds on the ice surface are covered by an ice-lid (Eicken, 2002). Snow may accumulate on the ice-lid, preventing further the detection of melt ponds from MODIS.

The simulated MP area fraction depends on the choice of reanalysis and melt pond scheme in this group of simulations. When forced by DFS, the seasonal maximum in MP area fraction is increased by 14 to 24 % compared to the corresponding simulations using JRA. The type of melt pond scheme leads to similar differences. The CESM scheme produces a maximum in MP area fraction 12 to 22 % larger than the one obtained with the topographic scheme when using JRA. The onsets of the melt ponds simulations are rather similar between the simulations. In autumn, however, the declines in MP area fractions happen at different rates. The decrease in MP area fraction is delayed by 6–7 days when using DFS and occurs at a faster rate with the CESM scheme than with the topographic scheme.

The spatial distributions of the mean MP area fractions during August over 2000–2011 are displayed in Fig. 2, for the group of simulations using T_{thr} equal to −0.15 °C. The simulations using the CESM scheme have a moderate spatial variability of MP area fraction in most of the Arctic basin. The Canadian Arctic Archipelago and the regions in its vicinity are exceptions. In these regions, the atmospheric forcing explains most of the differences in MP area fractions between the simulations. On the other hand, the simulations using the topographic scheme exhibit a more heterogeneous spatial variability of MP area fractions in the Arctic. The topographic scheme simulates larger MP area fractions in the Eurasian sector of the Arctic basin, irrespectively of the atmospheric forcing.

As comparison, Fig. 3 shows the corresponding MP area fractions from the datasets of Rösel et al. (2012) and Lee et al. (2020) in August over 2000–2011. Both datasets share spatial characteristics, although the spatial variability between the two is significantly different. The MP area fractions are maximum along the marginal ice zone, between 0.40 and 0.50 in Rösel et al.'s (Rösel et al., 2012) dataset, and up to 0.70 in Lee et al.'s (Lee et al., 2020) dataset. Additionally, the MP area fractions are smaller in the north of the Greenland coast. This region with smaller MP area fractions extends in the Arctic basin towards the North Pole in Rösel et al.'s (Rösel et al., 2012) dataset. On the opposite, Lee et al. (2020)'s dataset presents an increase in the spatial variability in the regions around the North Pole. The regions with smaller MP area fractions extend to the northern part of the Canadian Archipelago in this dataset.

The spatial variability of the MP area fraction as simulated by the topographic scheme can be related to the variability of the exposed MP area fraction presented by Flocco et al. (2012, Figure 4c). In this study, the atmospheric state is prescribed by DFS version 4.1, a former version of our DFS product. We find larger MP area fractions in the Canadian Arctic Archipelago as in Flocco et al. (2012) when using DFS version 5.2 compared to JRA.

The moderate spatial variability of the MP area fraction simulated by the CESM scheme differs from the observations shown in Fig. 3, but also to the model results of Zhang et al. (2018). These authors adjusted the aspect ratio relation of the CESM scheme to increase the melt pond depth over thicker ice. The range of MP area fractions in the Arctic basin as simulated by the CESM scheme and forced by JRA is comparable to the MP fractions from the control simulation of Zhang et al. (2018). Thus, the lack of spatial variability of the MP area fractions is likely due to the restrictive aspect ratio definition of the CESM scheme.

In-situ measurements of melt pond areas show a wide range of values (Polashenski et al., 2012, see Figure 1). In addition, melt ponds tend to cover a fraction of 0.30 of sea ice area on MYI, or between 0.40 to 0.60, up to 0.90 on FYI (Fetterer and Untersteiner, 1998). Melt ponds undergo significant interannual and spatial variations. In the region of the SHEBA 1998 campaign, whose measurements were used to set up the CESM scheme, Webster et al. (2015) estimated the maximum MP area fraction during the year 2011 as 0.38 and 0.53 on MYI and FYI, respectively. Perovich (2003) reported a mean value of 0.24 during SHEBA.

As shown in Fig. 4, the simulated volume of meltwater per sea ice area in melt ponds, or MP volume per ice area, progressively increases during the melt season as the meltwater accumulates in melt ponds, for simulations with T_{thr} equal to −0.15 °C. The seasonal maxima in MP

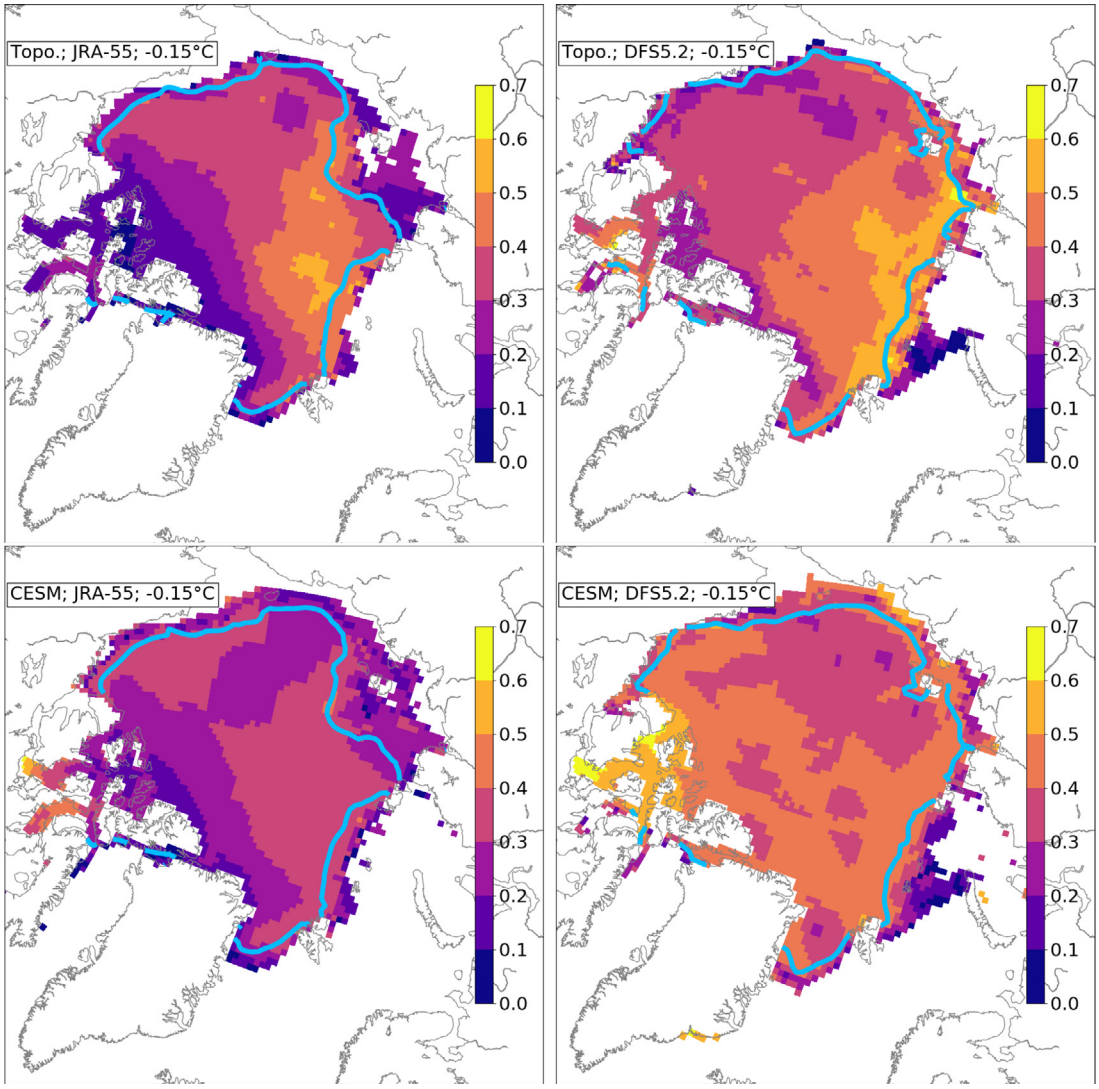

Fig. 2. Melt pond area fractions (of sea ice area) averaged in August over the period 2000–2011 for the simulations combining the topographic scheme (top row) and the CESM scheme (bottom row) with JRA (left column) and DFS (right column) as for the prescribed atmospheric surface states. The temperature threshold T_{thr} is equal to −0.15 °C in these four simulations. The light blue lines indicate the 15 % ice concentration contour.

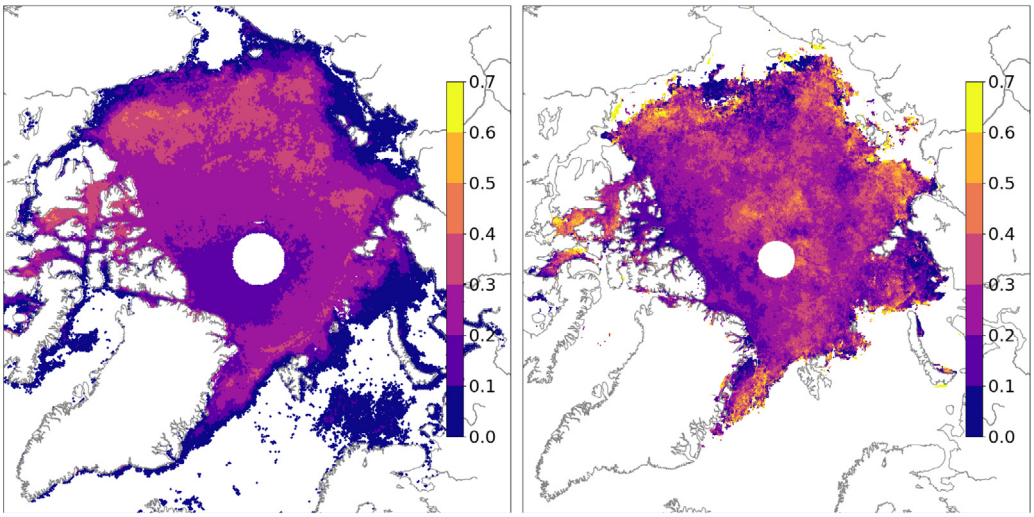

Fig. 3. Melt pond area fractions (of sea ice area) averaged in August over the period 2000–2011 for the observational products of Rösel et al. (2012) (left) and Lee et al. (2020) (right).

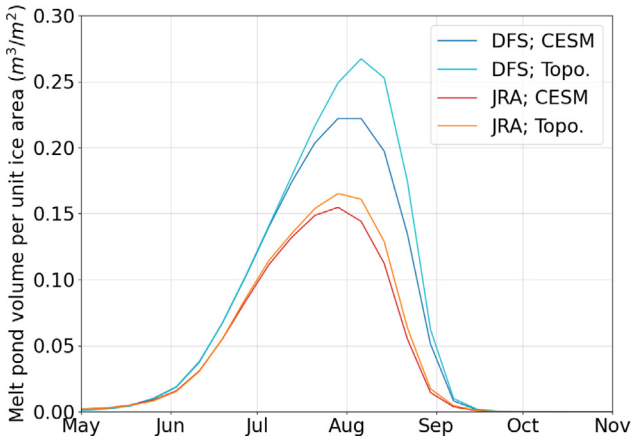

Fig. 4. Mean seasonal cycles of the melt pond volume of meltwater per sea ice area, averaged between 2000 and 2011 in the Northern Hemisphere where the ice concentration is strictly positive. The group of simulations has T_{thr} set equal to −0.15 °C.

volume per ice area are reached at the end of July and the beginning of August. In September, the volume of melt ponds is close to zero.

The seasonal maximum in MP volume per ice area is mostly set by the forcing. Simulations forced by DFS have greater MP volumes per ice area than the corresponding simulations forced by JRA. The seasonal maximum in MP volume per ice area ranges between 0.22 to 0.26 m^3 per sea ice area when using DFS, against 0.15 to 0.16 m^3 per sea ice area with JRA. The type of scheme has a weaker effect on the MP volume per ice area, with a slightly larger MP volume per ice area simulated by the topographic scheme than by the CESM scheme.

The mean melt pond depth is controlled by both the aspect ratio of melt ponds and the MP volume. The DFS forcing results in deeper melt ponds, with greater volume of meltwater and larger area fractions, because the difference of mean MP volume per ice area between the two forcing datasets exceeds the equivalent difference of mean MP area fractions. Melt ponds in simulations forced by DFS are between 44 and 59 cm deep on average in August, against 36 to 42 cm deep in simulations forced by JRA. On the contrary, the topographic scheme leads to MP volumes per ice area that are 7 to 20 % larger than the CESM scheme. However, the MP area fractions are 2 to 7 % smaller with the topographic scheme than with the CESM one. Thus, the topographic scheme simulates deeper melt ponds but covering smaller fractions of sea ice area, for notably larger MP volume per ice area, compared to the CESM scheme. In August, the melt ponds simulated by the topographic scheme are 6 to 15 cm deeper on average than those generated by the CESM scheme.

Large-scale and long-term observations of melt pond depth or volume do not exist. Observations of the deepening of melt ponds collected during SHEBA show peaks of 40 cm in early August (Perovich, 2003). Additionally, Morassutti and Ledrew (1996) analysed an ensemble of 504 measurements collected in the Canadian Arctic Archipelago over three ice surfaces. The mean depth of 31.0 cm is reported for melt ponds over MYI and 27.4 cm over land fast ice made from broken and deformed ice slabs driven against the coast. These mean depths contrast with the mean value of 13.0 cm on FYI. The ensemble of measurements has a large standard deviation of 16.2 cm and a maximum depth of 86 cm is recorded.

The atmospheric surface state is the main driver of the melting of the snow and ice surface layers, and subsequently of the spatial distribution of the MP volume per grid cell area. When normalising the simulated MP volume per grid cell area by the ice area, the effect of the atmospheric state is still visible on the spatial distribution of the MP volume per ice area (Fig. 5). In simulations forced by DFS, the spatial variability of the MP volume per ice area is small in the Arctic, for the reason that the spatial distribution of the MP volume per grid cell area matches approximately the gradient of ice concentration across the Arctic basin. The larger MP volumes per ice area along the 15 % concentration lines when associating DFS with the topographic scheme indicate the ability of this scheme to modulate the MP volume on the ice surface. This ability of the topographic scheme can also be seen in the simulations forced by DFS. The MP volume per ice area is spatially more heterogeneous when using the topographic scheme against the CESM scheme.

Fig. 6 presents the differences in SAT between DFS and JRA during summer, averaged between 2000 and 2011. The SAT is significantly larger in DFS than in JRA in the interior of the Arctic basin. The differences reach approximately 3.0 °C locally in two regions of the central Arctic. Otherwise, the SAT in DFS is lower than JRA 1.0 °C to 1.5 °C in the Barents and Norwegian Seas, as well as the southern part of the Kara Sea. The higher temperatures in DFS result in a more efficient melting of the snow surface layer and then of the ice surface layer.

In conclusion to this section, the seasonal cycles of the melt ponds are reasonably well reproduced by NEMO–LIM with T_{thr} set equal to −0.15 °C, especially the timing of the melt pond onset and the general shapes of the seasonal cycle. The simulated seasonal maximum in MP area fraction is overestimated compared to observations (Rösel et al., 2012; Lee et al., 2020) and other modelling studies using the ice-lid refreezing formulation (Flocco et al., 2012; Schröder et al., 2014; Lecomte et al., 2015). The ice-lid allows representing the exposed area fraction of MP in the model, which has a closer correspondence with the MP area fractions derived from MODIS. Melt ponds exhibit a strong sensitivity to the choice of the atmospheric forcing dataset, with greater melt pond volumes, area fractions and effective depths, when selecting DFS instead of JRA. The sensitivity of the simulated melt pond volume is likely due to the larger SATs over Arctic sea ice-covered regions during summer in DFS compared to JRA. On the other hand, the type of melt pond scheme impacts the aspect ratio of the melt ponds, with deeper and smaller area extents of melt ponds when using the topographic scheme than with the CESM scheme.

3.2. Impact of the refreezing temperature on the melt ponds

Among the three sources of uncertainty we have been considering, the value chosen for the refreezing temperature of melt ponds has the strongest impact on the seasonal evolution of these features. In this section, we analyse the simulations conducted with T_{thr} set equal to −2.00 °C. This value has been selected by Holland et al. (2012) and Zhang et al. (2018) to allow a realistic freeze-up of melt ponds in autumn in their model configurations. This lower threshold for the surface temperature can be associated with saline melt ponds and low freezing rates of melt ponds. Important intrusions of seawater in melt ponds can occur when melt ponds are connected to the ocean, either laterally through inter-connected melt ponds or vertically (Perovich et al., 2009).

Fig. 7 shows the mean seasonal cycles of the MP area fraction from the group of simulations with T_{thr} equal to −2.00 °C. The maximum in mean MP area fraction exhibits two distinct regimes depending on the type of melt pond scheme, nearly independently of the atmospheric forcing. More importantly, melt ponds are still present on sea ice in mid-September. The issue is particularly acute with the topographic scheme, where the refreezing is delayed by about one month.

As shown in Fig. 8, the mean seasonal cycle of the water depth in the melt ponds is also largely affected by the value chosen for T_{thr}. With T_{thr} = −0.15 °C, the mean melt pond depths are sensitive to the choice of melt pond scheme and atmospheric forcing dataset. When T_{thr} = −2.00 °C, the type of melt pond scheme plays a dominant role in the seasonal deepening of melt ponds. The simulations using the topographic scheme have greater mean depths (up to 90 cm) than with the CESM scheme (50 cm). Lastly, the seasonal maximum is delayed to late August and the decrease in pond depth is postponed to September and October.

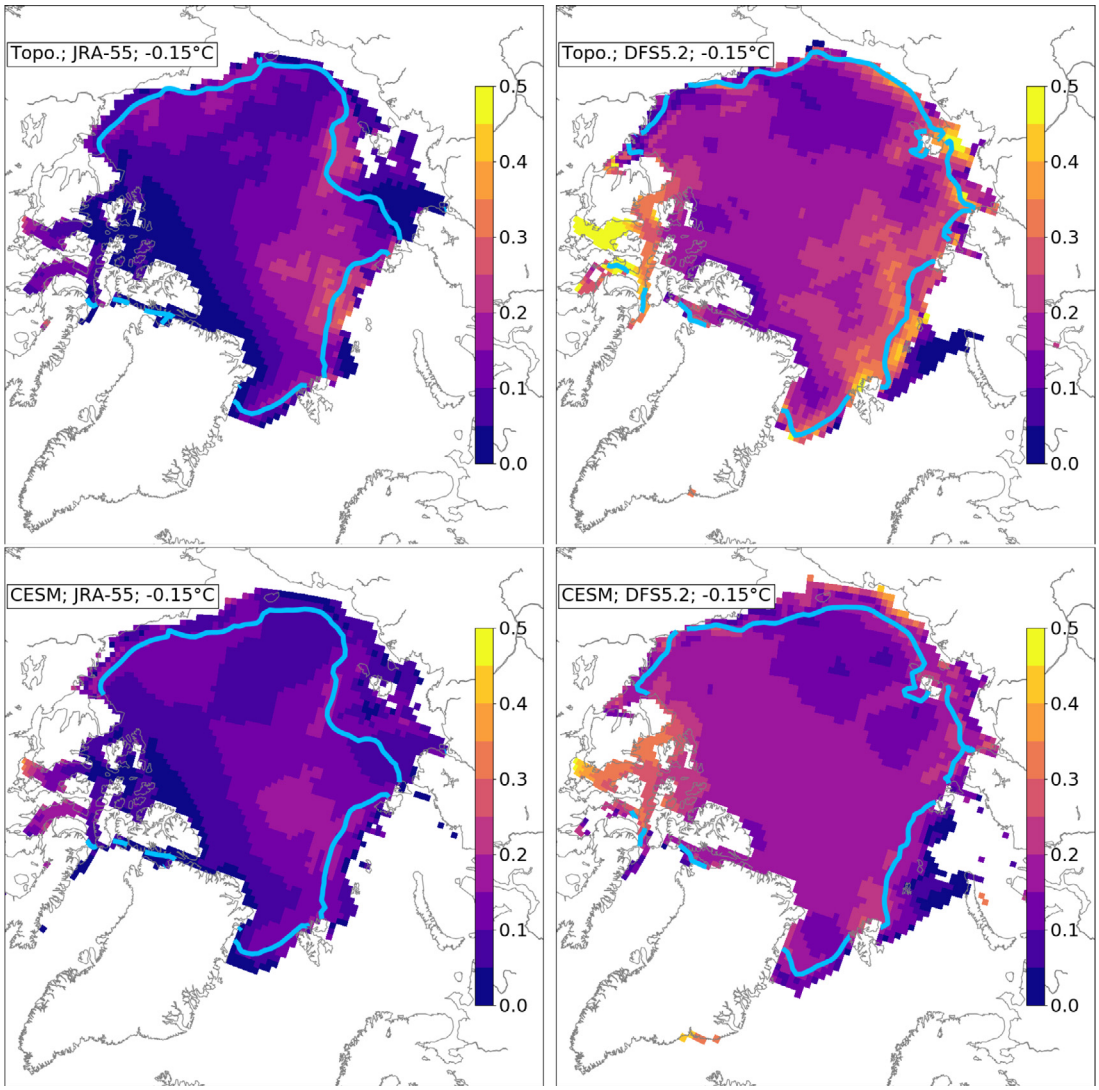

Fig. 5. Melt pond volume per ice area (m^3/m^2) averaged in August over the period 2000–2011 for the simulations combining the topographic scheme (top row) and the CESM scheme (bottom row) with JRA (left column) and DFS (right column) as for the prescribed atmospheric surface state. The temperature threshold T_{thr} is equal to −0.15 °C in these four simulations. The light blue lines indicate the 15 % ice concentration contour.

The number of days with SAT below the temperature threshold T_{thr} changes significantly depending on the value of the threshold itself. On average in August, there are 10 to 15 days with the SAT below −0.15 °C, whereas only 1 to 5 days have the SAT below −2.00 °C. Secondly, the refreezing mechanism leads to a faster refreezing of melt ponds when $T_{thr} = -0.15$ °C. Indeed, T_{thr} sets in part the exponential rate of Eq. (2) when melt ponds refreeze. Thus, the refreezing of melt ponds occurs at a faster rate and over a longer time with T_{thr} set equal to −0.15 °C than when set with −2.00 °C.

In autumn, the changes in the melt pond quantities are either due to meltwater losses or transformations of the sea ice state. The meltwater losses occur mainly through the refreezing of melt ponds because sea ice begins to grow again. Meltwater losses due to ridging and rafting events are also limited at this time of the year. The formation of new thin sea ice through thermodynamic processes has the effect of introducing ice in the small thickness categories of the ITD. The topographic scheme redistributes the remaining meltwater volume over these new thin ice categories, which maintains large melt pond area fractions. The change in ITD and the redistribution of meltwater are confirmed by the decrease in mean melt pond depth in Fig. 8. On contrary, the CESM scheme is largely unaffected by the growth of thin ice. The CESM scheme derives the ponded ice area and depth using the fixed aspect ratio, more independently to the sea ice state.

The refreezing of melt ponds is also active in spring and determines in part the onset of the melt ponds. The numbers of days below the threshold temperatures −2.00 °C and −0.15 °C begin to differentiate in June. The number of days with SAT less than −0.15 °C is between 7 to 15 days, against less than 4 days with SAT less than −2.00 °C. This difference in the numbers of days explains the slightly earlier onset of melt ponds in the group of simulations using T_{thr} set equal to −2.00 °C.

In July, the refreezing mechanism cannot explain the changes in melt pond quantities, since the average day with freezing conditions for melt ponds is too small. Meltwater losses are most likely due to the melting of the ice categories. The basal melt accounts for two-third and the surface ice melt for one-third of the total mass change in sea ice during July. These two processes exclude other factors of change in sea ice mass in the model. Thus, as sea ice is melting, the melt pond schemes flush the meltwater out to the ocean when the ice cover becomes too weakened. In addition to meltwater losses, the melting and disappearance of the thin ice categories lead to an increase in mean effective ice thickness. When redistributing the meltwater, the topographic scheme simulates deeper but smaller melt ponds than the CESM scheme.

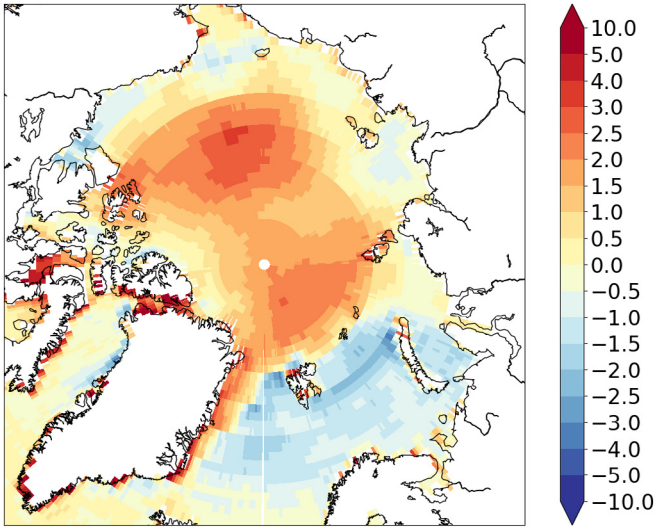

Fig. 6. Differences in SAT (°C) between the DFS and JRA atmospheric products, averaged from June to August over 2000–2011. Red (blue) colours indicate higher (lower) temperatures in DFS than JRA.

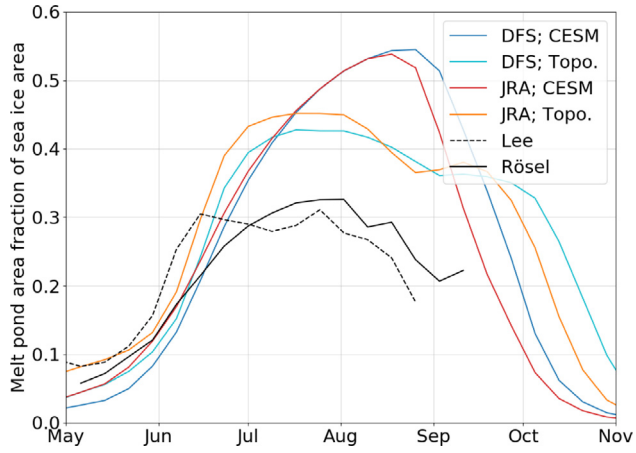

Fig. 7. As Fig. 1 but for the group of simulations with T_{thr} set equal to −2.00 °C. The mean seasonal cycles derived from the datasets of Rösel et al. (2012) and Lee et al. (2020) are drawn in black.

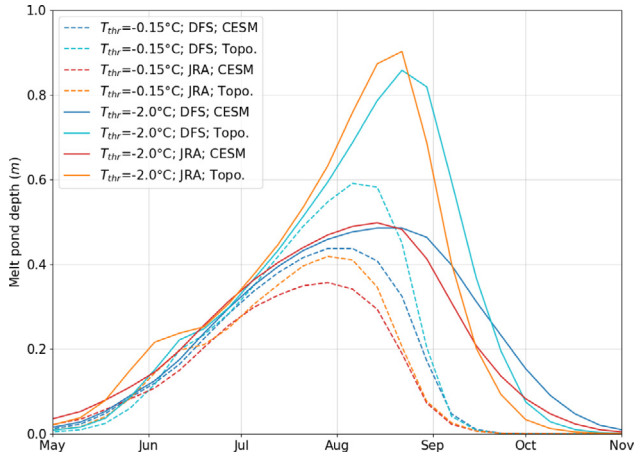

Fig. 8. Mean seasonal cycles of the effective meltwater depth in the melt ponds over 2000–2011 for the different simulations carried out with NEMO–LIM.

3.3. Trends in melt ponds characteristics

Trends in melt pond quantities over the past decades are computed between 1980 and 2015 in a similar way to Zhang et al. (2018) and Schröder et al. (2014) (Table 2). To account for the negative trends in sea ice area from the mass fluxes, we normalised the time series by the total sea ice area. Similarly, we computed the trends in the mean melt pond area and volume per sea ice area.

The trends in total Arctic sea ice area (SIA) are negative during all months in each of the simulations over the period 1980 to 2015. The reductions in total SIA in the simulations are consistent with the observed changes in Arctic ice extent over the past decades (Serreze and Meier, 2018). Between June and August, the modelled trend in total SIA ranges between -0.59×10^6 and -0.65×10^6 km^2 per decade, which corresponds to a difference of 9 %. The trend in SIA derived from the NSIDC-0051 product is -0.69×10^6 km^2 per decade.

Positive trends in MP area and volume per sea ice area ice are observed in all simulations. On the one hand, the simulations combining the CESM scheme with $T_{thr} = -2.00$ °C have small and statistically insignificant trends in MP area and volume per sea ice area. In comparison, Zhang et al. (2018) found insignificant small downward trends in MP area and volume per sea ice area. Zhang et al. (2018) made use of a modified version of the CESM scheme, the same refreezing mechanism used in our study and $T_{thr} = -2.00$ °C. On the other hand, simulations using the topographic scheme and T_{thr} set equal to −0.15 °C have significant positive trends in MP area and volume per sea ice area. The sign of the trend in MP area fraction in these two simulations agrees with Schröder et al. (2014), who found a positive trend over a similar period of time with the topographic scheme and an ice-lid refreezing formulation (Flocco et al., 2010).

The trend in the total mass flux of meltwater entering the ponds per ice area increase in all the simulations. However, none of the trends is statistically significant. In comparison, the trends in total meltwater mass fluxes per ice area leaving the melt ponds are slightly larger than the corresponding mass fluxes entering the melt ponds, except for one simulation that combines the topographic melt pond scheme with DFS and $T_{thr} = -2.00$ °C. The slight imbalance should lead to a negative trend in MP area and volume per sea ice area, in contradiction with the calculated positive trend in MP area and volume per sea ice area. Only simulations using T_{thr} equal to −2.00 °C have statistically significant trends. More statistical significance could be gained by integrating the mass fluxes over the whole period the surface melting is active.

The slight imbalance in total mass fluxes entering and leaving the melt ponds per ice area, as well as the absence of strong statistical significance, suggest a role of the sea ice state for the melt pond evolution over the past decades, rather than strong changes in the meltwater fluxes in and out of the melt ponds. The Arctic sea ice has been transitioning towards a more seasonal and thinner state during the recent decades. These transitions have a direct effect on the ITD and consequently on the derivation of melt ponds by the topographic scheme. In addition, the CESM scheme relies on the ice concentration to estimate the MP area and volume per sea ice area. The local changes in sea ice concentration impact the derivation of melt ponds quantities by the CESM scheme.

3.4. Impact on the arctic sea ice

3.4.1. Sea ice extent

NEMO–LIM reproduces most of the characteristics of the mean seasonal cycle of the Arctic sea ice extent derived from NSIDC-0051 (Fig. 9(a)). In winter, the rate of change in sea ice extent is close to NSIDC-0051 and the seasonal maximum occurs comparably in March for all simulations. During this month, the sea ice extent simulated by NEMO–LIM is 5 % larger than NSIDC-0051. The position of the ice edge (ice concentration equal to 15 %) is not well represented in some parts of the Arctic. This misplacement can be quantified by the integrated

Table 2
Trends in total Arctic sea ice area (SIA) (10^6 km^2 per decade), total volume of meltwater per day entering ϕ_{in}^{pnd} and leaving ϕ_{out}^{pnd} the melt ponds normalised by the SIA (mm/month per decade), mean melt pond area fraction of sea ice (% per decade) and mean melt pond volume per ice area (cm per decade), over 1980 to 2015 averaged over June, July and August. Values in bold fonts have a p-value less than 0.05.

T_{thr} °C	Scheme	Forcing	SIA 10^6 km^2	ϕ_{in}^{pnd} mm/mon	ϕ_{out}^{pnd} mm/mon	$\frac{A_{pnd}}{A_{ice}}$ %	$\frac{V_{pnd}}{S_{ice}}$ cm
−0 15	Topo.	DFS	**−0.59**	5.53	10.75	**1.89**	**1.27**
−0 15	Topo.	JRA	**−0.63**	5.29	12.27	**1.94**	**1.44**
−0 15	CESM	DFS	**−0.61**	7.46	16.08	1.29	0.79
−0 15	CESM	JRA	**−0.64**	6.90	16.90	**1.97**	**1.14**
−2 00	Topo.	DFS	**−0.60**	5.71	**4.30**	**1.60**	1.44
−2 00	Topo.	JRA	**−0.65**	6.13	**11.16**	1.45	1.53
−2 00	CESM	DFS	**−0.62**	7.66	**17.05**	1.01	0.77
−2 00	CESM	JRA	**−0.65**	7.28	**19.99**	0.95	0.79

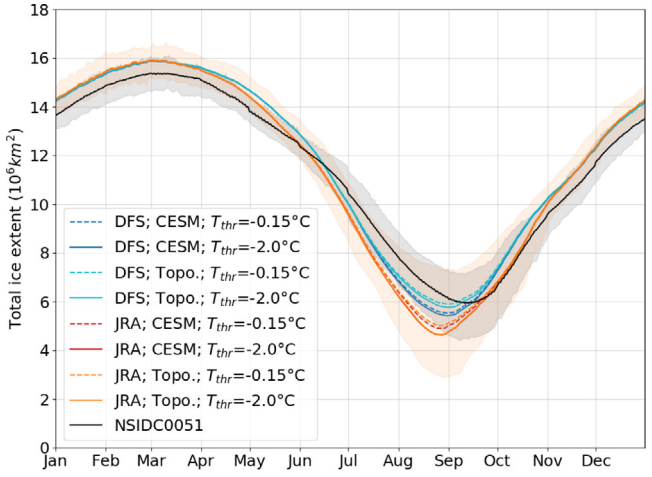

(a) Arctic sea ice extent

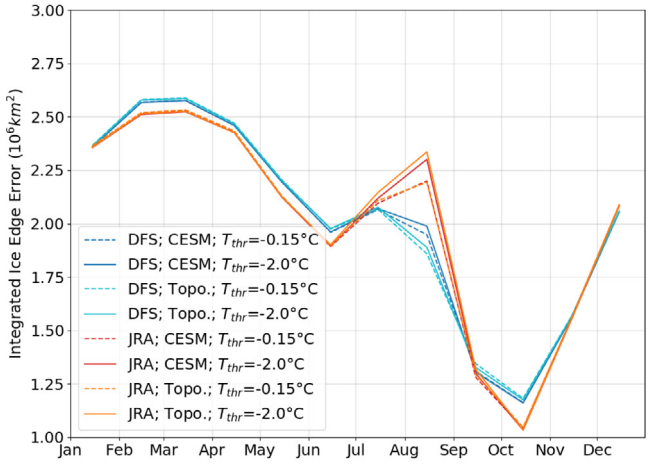

(b) Integrated ice edge error

Fig. 9. Mean seasonal cycles of total Arctic sea ice extent (9(a)) and integrated ice edge error (9(b)) over 1980–2015. Simulations are given a colour as a function of the atmospheric product (warm-cold), melt pond scheme (light-dark) and a line style following T_{thr} (continuous-dashed). NSIDC-0051 is drawn in black and the grey shaded area shows the ice extents between the 10th and 90th percentiles. Similarly, the orange shaded area is enclosed by lowest 10th and highest 90th percentiles of sea ice extents from the set of simulations. The integrated ice edge error is calculated against NSIDC-0051.

ice edge error (IIEE) (Goessling et al., 2016). IIEE corresponds to the symmetric difference between the areas enclosed by the modelled and observed sea ice edges. Fig. 9(b) depicts the mean seasonal cycles of the IIEE for all the simulations, using NSIDC-0051 as the reference product. The IIEEs are maximum in March and result from too large sea ice concentrations in the Labrador and Greenland Seas and too low ice concentrations in the regions of the North Pacific and the Gulf of Saint Lawrence.

In summer, NEMO–LIM simulates a minimum ice extent that occurs two to three weeks in advance compared to NSIDC-0051. Such early summer minimum ice extents are common to studies using similar model set-ups (Rousset et al., 2015; Lecomte et al., 2015; Docquier et al., 2017). In September, the sea ice concentrations are 4 to 8 % larger than the NSIDC-0051 values in the central Arctic. In the regions of the Barents, Kara and Laptev Seas, the model underestimates the ice concentration by 10 % to 20 %, whereas the ice concentrations are overestimated in the Canadian Arctic Archipelago and Fram Strait by up to 30 to 60 %.

The differences between the simulations accentuate during summer in terms of sea ice extent and IIEE. The group of simulations using DFS has a smaller IIEE and a minimum sea ice extent closer to NSIDC-0051, compared to the group using JRA. For the same atmospheric product and melt pond scheme, the IIEE is reduced when T_{thr} is equal to −0.15 °C. Regarding the type of scheme, the differences are less clear. Simulations combining JRA and $T_{thr} = -2.00$ °C show no differences in mean ice extent and little changes in IIEE. With DFS, the topographic scheme improves the simulation of the ice extent and the position of the ice edge. In winter, the differences between the simulations are less important and can be attributed essentially to the atmospheric forcing dataset. From January to June, the simulations have larger IIEEs with DFS than with JRA.

3.4.2. Sea ice volume

The mean seasonal cycles of the total sea ice volume simulated by NEMO–LIM compare relatively well with the PIOMAS reanalysis (Fig. 10). The modelled Arctic sea ice volume is 0.6×10^3 to 4.0×10^3 km^3 larger than the PIOMAS product from August to January. During these months, the monthly means of the simulated sea ice volume are within the 10th and 90th percentiles of the seasonal cycles of sea ice volume from PIOMAS. Then, the gap between NEMO–LIM and PIOMAS increases up to 4.9×10^3 and 6.7×10^3 km^3 in May. From March to June, the monthly means of the simulated sea ice volume exceed the 90th percentile from the PIOMAS reanalysis. However, one must keep in mind that Schweiger et al. (2011) estimated the uncertainty of PIOMAS Arctic sea ice volume as 1.35×10^3 km^3 in October and 2.25×10^3 km^3 in March.

The timings of the seasonal extremes in sea ice volume are relatively in phase between the simulations and PIOMAS. The maximum is reached at the end of April in NEMO–LIM, about 10 days later than in PIOMAS, whereas the minimum occurs 6 to 8 days before the PIOMAS one, in September. From May to July, the seasonal loss of Arctic sea ice volume is faster than PIOMAS. Seasonal maxima and minima are slightly smaller than the values documented by Rousset et al. (2015). In their study, the effect of melt ponds is considered implicitly using a constant lower albedo value for bare ice, when the ice surface temperature is above the melting point.

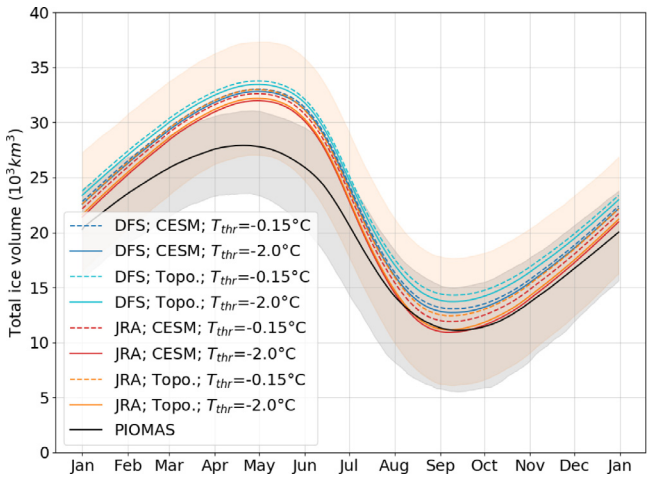

Fig. 10. Mean seasonal cycles of the total Arctic sea ice volume over 1980–2015 from NEMO–LIM (in colours) and PIOMAS (in black). The grey shaded area is enclosed by the 10th and 90th percentiles of the total sea ice volume from PIOMAS. Similarly, the orange shaded area is enclosed by the lowest 10th percentile and the highest 90th percentile of the set of simulations from NEMO–LIM. Simulations are given a colour as a function of the atmospheric dataset (warm-cold), melt pond scheme (light-dark) and a line style following T_{thr} (continuous-dashed).

The differences in Arctic sea ice volume between the simulations are sustained all year round. The range of mean seasonal Arctic ice volume simulated by NEMO–LIM is not constant between the months, from $1.9 \times 10^3\,\mathrm{km}^3$ in May to $3.3 \times 10^3\,\mathrm{km}^3$ in August. When pairing the simulations, we find that simulations using DFS, the topographic scheme, and T_{thr} equal to $-0.15\,°\mathrm{C}$, tends to have greater Arctic sea ice volume than the respective simulations using JRA, the CESM scheme, and T_{thr} equal to $-2.00\,°\mathrm{C}$.

3.5. Difference in the representation of the sea ice in the simulations

To investigate further the differences between the simulations, we introduce the mean absolute difference (D) as the absolute difference between two variables following one change in the experimental set-up (atmospheric forcing or refreezing temperature or melt pond scheme) while keeping the other two elements identical. The simulations can be thought as representations of the same climate system, and the differences between them as distances expressing the disagreement of the simulations on the representation of the climate state. By carefully selecting simulations and comparing the differences, we can examine specific aspects of the model formulation. For instance, to study the impact of differences due to the CESM and topographic schemes, simulations can be paired by the type of scheme, with pairs using the same atmospheric forcing dataset and T_{thr} value. Then, we can calculate the mean absolute difference between the pairs of simulations. The mean absolute difference related to the type of scheme, choice of atmospheric forcing dataset and refreezing temperature are referred to D_{scheme}, $D_{forcing}$ and D_{Tthr}, respectively.

In the central Arctic, the distance $D_{forcing}$ attributed to the atmospheric forcing explains most of the differences in mean sea ice volume between the simulations (Fig. 11). The contribution north of Greenland and the Canadian Arctic Archipelago is comparatively smaller than most of the other regions of the ice pack. The effect of the atmosphere forcing on the differences is more important in the Beaufort and Chukchi Seas and the area north of the Barents Sea. There, $D_{forcing}$ is about $0.60\,\mathrm{m}^3/\mathrm{m}^2$ on average. $D_{forcing}$ is much larger in the Canadian Arctic Archipelago, where the variable peaks at $4.63\,\mathrm{m}^3/\mathrm{m}^2$.

In comparison, the distances D_{scheme} and D_{Thr} attributed to the type of scheme and refreezing temperature are much smaller. D_{Thr} is near zero in the Eurasian sector of the Arctic, but this diagnostic amounts to $0.24\,\mathrm{m}^3/\mathrm{m}^2$ in the Beaufort and Chukchi Seas. D_{scheme} is within a similar interval, though smaller in value, to $D_{forcing}$. The most important distance of D_{scheme} lies in the Canadian Arctic Archipelago, where it reaches $1.61\,\mathrm{m}^3/\mathrm{m}^2$, a value similar to that of $D_{forcing}$. The differences are lower in the central Arctic Ocean. Distances due to the type of scheme greater than $0.8\,\mathrm{m}^3/\mathrm{m}^2$ are restricted to the Beaufort, Chukchi and East Siberian Seas.

In their current implementation in NEMO–LIM, melt ponds interact with the sea ice and ocean systems through two mechanisms. Firstly, melt ponds alter the surface albedo through the melt pond area fraction and the effective depth of meltwater present in the melt ponds (see Eq. (3)). When melt ponds deepen, the albedo quickly decreases towards the minimum albedo of ponded ice surfaces. A melt pond depth greater than 23 cm results in a ∼99 % decrease in the albedo of melt ponds relative to the nominal value. Thus, Eq. (3) inhibits strongly the effect of excessively deep melt ponds on the area-averaged surface albedo. Secondly, melt ponds interact with the ocean surface layer through the mass fluxes of freshwater, by delaying the input of surface meltwater during the melt season. The amount of meltwater in the melt ponds is mostly set by the atmospheric forcing dataset, rather than by the type of melt pond scheme or value for T_{thr}. Consequently, the effects of the uncertainties in the melt pond formulation through the mass fluxes of freshwater on the sea ice volume are weak compared to the uncertainties in the atmospheric state.

The mean absolute differences of sea ice volume tell us that having an accurate representation of the surface atmospheric state is key to better simulate the Arctic sea ice volume. Our results suggest that the sea ice state (volume and area) is primarily impacted by changes in the atmospheric forcing, and to a much lesser degree by changes in the melt pond scheme formulation and value for the refreezing temperature. This result is in line with that of Hunke (2010), who found a dominant effect of changes in atmospheric and oceanic external forcings. Consequently, despite its relative simplicity, the CESM melt pond scheme leads to results that are rather similar to those obtained with the topographic scheme. Lastly, the freezing point of melt ponds also leads to small effects on the simulated sea ice volume, comparatively to the atmospheric forcing. However, our simulations using $-2.00\,°\mathrm{C}$ have consistently lower sea ice quantities, a larger IIEE and an unrealistic melt pond freeze-up. We find a better agreement with observations when using the value of $-0.15\,°\mathrm{C}$ for T_{thr} in Eq. (2) with our current model set-up

4. Conclusion

In this study, we have run the global ocean–ice model NEMO–LIM with two conceptually different melt pond schemes, two prescribed refreezing temperatures for melt ponds and two atmospheric forcing datasets. We have examined the differences between the simulations to investigate the effect of the uncertainties in the formulation of melt ponds and the atmospheric state, in a realistic set-up. As a reference and to guide the climate modelling community, our main findings are summarised in Table 3.

Melt ponds contain at least small amounts of salt due to the melting of sea ice. Towards the end of the melt season, the salinity in melt ponds can be large if melt ponds are connected to the ocean. Consequently, the refreezing temperature of melt ponds is in-between the freezing points of seawater and freshwater. We have shown that the value of $-2.00\,°\mathrm{C}$ leads to unrealistic seasonal cycles of the mean melt pond area fraction in our set-up. Moreover, the simulated maxima in melt ponds area fractions can be quite large compared to observational datasets (Rösel et al., 2012; Lee et al., 2020).

The overestimation of ponded ice area occurs also with the more realistic temperature threshold of $-0.15\,°\mathrm{C}$. This suggests that important processes are not resolved by our current implementation of melt ponds, such as the development of ice-lids during freeze-up (Flocco et al., 2010). The thermal evolution of melt ponds is highly dependent

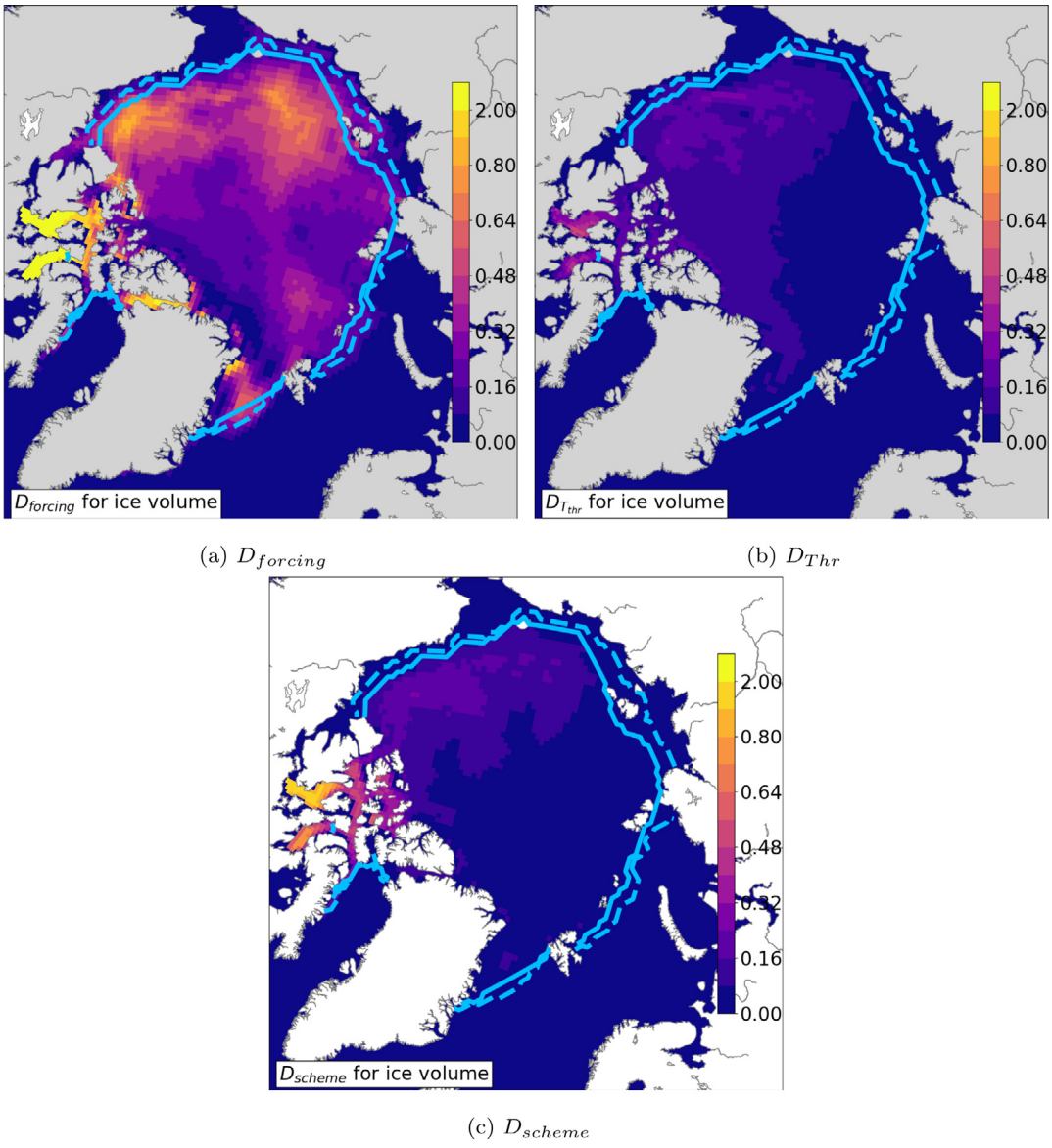

(a) $D_{forcing}$ (b) D_{Thr}

(c) D_{scheme}

Fig. 11. Mean absolute differences of sea ice volume attributed to the forcing (11(a)), T_{thr} (11(b)) and melt pond scheme (11(c)) in September over 1980–2011, in m^3 per grid cell area. The light blue continuous (dashed) line indicates the 15 % ice concentration contour of the simulation with the smallest (largest) ice extent.

Table 3
Summary of the effects of the type of melt pond scheme, choice of the refreezing temperature for melt ponds and uncertainties in the atmospheric state on the simulated melt ponds and sea ice quantities in the Arctic.

	Melt ponds	Sea ice
Aspect ratio definition	Smaller but deeper melt ponds with the topographic scheme	Small effects mostly seen in the Canadian Arctic Archipelago and parts of the Beaufort and Chukchi Seas
Refreezing temperature of melt ponds	Dominant effect of T_{thr}: −2 00 °C leads to unrealistic refreezing of melt ponds and accentuates the difference in aspect ratios between the schemes	Small effects mostly in the Beaufort and Chukchi Seas
Atmospheric forcing dataset	Deeper melt ponds and delayed refreezing with DFS than with JRA	Dominant effect of the forcing on the Arctic sea ice

on the salt and heat content as well as on the stratification of the water column in melt ponds (Kim et al., 2018). Furthermore, the effect of the ice salinity on the permeability of the ice is not fully resolved by the schemes. In the topographic scheme, the water seepage due to the porosity of the ice is computed from Darcy's law using the internal ice temperature (Assur, 1958; Notz, 2005; Golden et al., 2007). However, meltwater seeping through the ice structure may refreeze and alter the ice permeability (Polashenski et al., 2012). These, in turn, control the level of water in the melt ponds, and consequently the volume of melt ponds and area fractions (Turner and Hunke, 2015). Thus, we

advocate a more comprehensive representation of such processes to better represent melt ponds in climate models (Flocco et al., 2016, withdrawn).

The second aspect of this study concerned the definition of the aspect ratio for the melt pond schemes. The explicit definition of the aspect ratio in the CESM scheme bounds the melt pond area fractions and depths to realistic values, even under nonphysical conditions such as when T_{thr} is equal to −2.00 °C. The CESM scheme leads to a moderate spatial variability of melt pond area fraction and volume per ice area. This indicates a lack of representativeness of such aspect ratio definition, either temporally (Webster et al., 2015) or spatially (Zhang et al., 2018). In contrast, the topographic scheme depends on the sea ice thickness distribution, which allows a more realistic representation of melt ponds with a greater degree of freedom. When T_{thr} is equal to −2.00 °C, the topographic scheme simulates more heterogeneous melt pond area fractions in autumn because of the changes in ice thickness distribution.

All simulations feature positive trends in melt pond area fractions and volumes per sea ice area. We have found significant positive trends in melt pond area fractions in the simulations using the topographic scheme and T_{thr} equal to −0.15 °C, in agreement with Schröder et al. (2014). However, we have also found non-significant small positive trends when using the CESM scheme with the lower value of −2.00 °C for T_{thr}, a result closer to the findings of Zhang et al. (2018). At this stage, the interpretation of the trends in normalised freshwater fluxes entering and leaving the melt ponds remains unclear because of the absence of statistical evidence. The differences between these trends suggest a role of the sea ice state for the evolutions of the melt pond area and volume over the past decades. The Arctic sea ice is transitioning towards more seasonal ice, which is thinner and less deformed, with a direct impact on the ITD and the melt ponds simulated by the topographic scheme. The CESM relies on a specific set of observations bounded in time and space, that are likely not fully representative of Arctic melt ponds over the past decades. With the recent introduction of new observational datasets such as those of Rösel et al. (2012) and Lee et al. (2020), the formulation of melt pond schemes could be refined and assessed more thoroughly to better account for changes in the sea ice state.

Uncertainty in the atmospheric state is the first cause of differences in Arctic sea ice volume in our simulations. In other words, the formulations of the topographic and CESM melt pond schemes, and also the values −0.15 °C and −2.00 °C for the freezing point of melt ponds, induce smaller effects on the sea ice state. Consequently, the relative simplicity of the CESM scheme can be considered as an advantage for climate models, as this formulation does not require to resolve the ice thickness distribution or fraction of level-ice. The explicit aspect ratio definition can also be easily adjusted (Zhang et al., 2018). General circulation models would benefit from more realistic melt pond schemes and refreezing formulations, notably for their effects on the freshwater fluxes between the ocean, melt ponds and ice systems, but also for their contribution to the form drag opposing the flow of air near the ice surface. These effects on the freshwater fluxes and atmospheric form drag will be the object of a future study.

Declaration of competing interest

The authors declare that they have no known competing financial interests or personal relationships that could have appeared to influence the work reported in this paper.

Acknowledgements

Computational resources have been provided by the supercomputing facilities of the Université catholique de Louvain (CISM/UCL) and the Consortium des Equipements de Calcul Intensif en Fédération Wallonie Bruxelles (CECI) funded by the F.R.S.-FNRS under convention 2.5020.11. François Massonnet is a F.R.S.-FNRS Research Associate. The research leading to these results has received funding from the European Commission's Horizon 2020 APPLICATE (GA 727862) and PRIMAVERA (GA 641727) projects. We also thank the anonymous reviewers for their valuable comments on an earlier version of this manuscript.

References

Arrigo, Kevin R., Perovich, Donald K., Pickart, Robert S., Brown, Zachary W., Van Dijken, Gert L., Lowry, Kate E., Mills, Matthew M., Palmer, Molly A., Balch, William M., Bahr, Frank, Bates, Nicholas R., Benitez-Nelson, Claudia, Bowler, Bruce, Brownlee, Emily, Ehn, Jens K., Frey, Karen E., Garley, Rebecca, Laney, Samuel R., Lubelczyk, Laura, Mathis, Jeremy, Matsuoka, Atsushi, Mitchell, B. Greg, Moore, G.W.K., Ortega-Retuerta, Eva, Pal, Sharmila, Polashenski, Chris M., Reynolds, Rick A., Schieber, Brian, Sosik, Heidi M., Stephens, Michael, Swift, James H., 2012. Massive phytoplankton blooms under Arctic sea ice. Science (ISSN: 10959203) 336 (6087), 1408. http://dx.doi.org/10.1126/science.1215065, URL http://www.sciencemag.org/cgi/doi/10.1126/science.1215065.

Assur, Andrew, 1958. Composition of sea ice and its tensile strength. Arct. Sea Ice 598, 106–138.

Barthélemy, Antoine, Goosse, Hugues, Fichefet, Thierry, Lecomte, Olivier, 2017. On the sensitivity of Antarctic sea ice model biases to atmospheric forcing uncertainties. Clim. Dynam. http://dx.doi.org/10.1007/s00382-017-3972-7.

Bintanja, R., Andry, O., 2017. Towards a rain-dominated Arctic. Nature Clim. Change 7 (4), 263–267. http://dx.doi.org/10.1038/nclimate3240, Publisher: Springer Science and Business Media LLC.

Bitz, C.M., Lipscomb, William H., 1999. An energy-conserving thermodynamic model of sea ice. J. Geophys. Res. Oceans 104 (C7), 15669–15677. http://dx.doi.org/10.1029/1999jc900100.

Blanke, Bruno, Delecluse, Pascale, 1993. Variability of the tropical atlantic ocean simulated by a general circulation model with two different mixed-layer physics. J. Phys. Oceanogr. 23 (7), 1363–1388. http://dx.doi.org/10.1175/1520-0485(1993)023<1363:vottao>2.0.co;2.

Bouillon, Sylvain, Morales Maqueda, M.A., Legat, Vincent, Fichefet, Thierry, 2009. An elastic-viscous-plastic sea ice model formulated on arakawa B and C grids. Ocean Model. (ISSN: 14635003) 27 (3–4), 174–184. http://dx.doi.org/10.1016/j.ocemod.2009.01.004.

Brodeau, Laurent, Barnier, Bernard, Treguier, Anne-Marie, Penduff, Thierry, Gulev, Sergei, 2010. An ERA40-based atmospheric forcing for global ocean circulation models. Ocean Model. 31 (3–4), 88–104. http://dx.doi.org/10.1016/j.ocemod.2009.10.005.

Cavalieri, Donald, 1996. Sea Ice Concentrations from Nimbus-7 SMMR and DMSP SSM/I-SSMIS Passive Microwave Data, Version 1. NASA National Snow and Ice Data Center Distributed Active Archive Center, http://dx.doi.org/10.5067/8gq8lzqvl0vl, URL http://nsidc.org/data/NSIDC-0051/versions/1.

Curry, Judith A., Schramm, Julie L., Ebert, Elizabeth E., 1995. Sea ice-albedo climate feedback mechanism. J. Clim. 8 (2), 240–247. http://dx.doi.org/10.1175/1520-0442(1995)008<0240:siacfm>2.0.co;2.

Dai, Aiguo, Trenberth, Kevin E., 2002. Estimates of freshwater discharge from continents: Latitudinal and seasonal variations. J. Hydrometeorol. 3 (6), 660–687. http://dx.doi.org/10.1175/1525-7541(2002)003<0660:eofdfc>2.0.co;2.

Dee, D.P., Uppala, S.M., Simmons, A.J., Berrisford, P., Poli, P., Kobayashi, S., Andrae, U., Balmaseda, M.A., Balsamo, G., Bauer, P., Bechtold, P., Beljaars, A.C.M., Berg, L. van de, Bidlot, J., Bormann, N., Delsol, C., Dragani, R., Fuentes, M., Geer, A.J., Haimberger, L., Healy, S.B., Hersbach, H., Hólm, E.V., Isaksen, L., allberg, P. K\textbackslashtextbackslasha, Köhler, M., Matricardi, M., McNally, A.P., Monge-Sanz, B.M., Morcrette, J.-J., Park, B.-K., Peubey, C., de Rosnay, P., Tavolato, C., Thépaut, J.-N., Vitart, F., 2011. The ERA-interim reanalysis: configuration and performance of the data assimilation system. Q. J. R. Meteorol. Soc. 137 (656), 553–597. http://dx.doi.org/10.1002/qj.828.

Depoorter, M.A., Bamber, J.L., Griggs, J.A., Lenaerts, J. T.M., Ligtenberg, S.R.M., Broeke, M.R. van den, Moholdt, G., 2013. Calving fluxes and basal melt rates of Antarctic ice shelves. Nature 502 (7469), 89–92. http://dx.doi.org/10.1038/nature12567.

Docquier, D., Massonnet, F., Barthélemy, A., Tandon, N.F., Lecomte, O., Fichefet, T., 2017. Relationships between Arctic sea ice drift and strength modelled by NEMO-LIM3.6. Cryosphere 11 (6), 2829–2846. http://dx.doi.org/10.5194/tc-11-2829-2017.

Dussin, Raphael, Barnier, Bernard, Brodeau, Laurent, Molines, Jean Marc, 2016. The making of Drakkar forcing set DFS5. DRAKKAR/MyOcean Report 01-04-16, LGGE, Grenoble, France.

Eicken, H., 2002. Tracer studies of pathways and rates of meltwater transport through Arctic summer sea ice. J. Geophys. Res. (ISSN: 0148-0227) 107 (C10), 8046. http://dx.doi.org/10.1029/2000JC000583.

Feltham, D.L., Untersteiner, N., Wettlaufer, J.S., Worster, M.G., 2006. Sea ice is a mushy layer. Geophys. Res. Lett. 33 (14), http://dx.doi.org/10.1029/2006gl026290.

Fetterer, Florence, Untersteiner, Norbert, 1998. Observations of melt ponds on Arctic sea ice. J. Geophys. Res. Oceans (ISSN: 21699291) 103 (C11), 24821–24835. http://dx.doi.org/10.1029/98JC02034.

Flocco, D., Feltham, D.L., 2007. A continuum model of melt pond evolution on Arctic sea ice. J. Geophys. Res. 112 (C8), http://dx.doi.org/10.1029/2006jc003836.

Flocco, D., Feltham, D.L., Bailey, E., Schroeder, D., 2015. The refreezing of melt ponds on Arctic sea ice. J. Geophys. Res. Oceans (ISSN: 21699291) 120 (2), 647–659. http://dx.doi.org/10.1002/2014JC010140.

Flocco, D., Feltham, D.L., Schroeder, D., Tsamados, M., 2016. Impact of refreezing melt ponds on Arctic sea ice basal growth. Cryosphere Discuss. 2016, 1–26. http://dx.doi.org/10.5194/tc-2016-118, URL https://tc.copernicus.org/preprints/tc-2016-118/.

Flocco, D., Feltham, D.L., Turner, A.K., 2010. Incorporation of a physically based melt pond scheme into the sea ice component of a climate model. J. Geophys. Res. 115 (C8), http://dx.doi.org/10.1029/2009jc005568.

Flocco, D., Schroeder, D., Feltham, D.L., Hunke, E.C., 2012. Impact of melt ponds on Arctic sea ice simulations from 1990 to 2007. J. Geophys. Res. Oceans 117 (C9), n/a–n/a. http://dx.doi.org/10.1029/2012jc008195.

Freitag, Johannes, Eicken, Hajo, 2003. Meltwater circulation and permeability of Arctic summer sea ice derived from hydrological field experiments. J. Glaciol. 49 (166), 349–358. http://dx.doi.org/10.3189/172756503781830601.

Frey, Karen E., Perovich, Donald K., Light, Bonnie, 2011. The spatial distribution of solar radiation under a melting Arctic sea ice cover. Geophys. Res. Lett. (ISSN: 00948276) 38 (22), n/a–n/a. http://dx.doi.org/10.1029/2011GL049421.

Goessling, H.F., Tietsche, S., Day, J.J., Hawkins, E., Jung, T., 2016. Predictability of the Arctic sea ice edge. Geophys. Res. Lett. 43 (4), 1642–1650. http://dx.doi.org/10.1002/2015gl067232.

Golden, K.M., Eicken, H., Heaton, A.L., Miner, J., Pringle, D.J., Zhu, J., 2007. Thermal evolution of permeability and microstructure in sea ice. Geophys. Res. Lett. 34 (16), http://dx.doi.org/10.1029/2007gl030447.

Grenfell, Thomas C., 2004. Seasonal and spatial evolution of albedo in a snow-ice-land-ocean environment. J. Geophys. Res. 109 (C1), http://dx.doi.org/10.1029/2003jc001866.

Holland, Marika M., Bailey, David A., Briegleb, Bruce P., Light, Bonnie, Hunke, Elizabeth, 2012. Improved sea ice shortwave radiation physics in CCSM4: The impact of melt ponds and aerosols on Arctic sea ice. J. Clim. (ISSN: 08948755) 25 (5), 1413–1430. http://dx.doi.org/10.1175/jcli-d-11-00078.1.

Hunke, Elizabeth C., 2010. Thickness sensitivities in the CICE sea ice model. Ocean Model. 34 (3–4), 137–149. http://dx.doi.org/10.1016/j.ocemod.2010.05.004.

Hunke, E., Allard, R., Bailey, D.A., Blain, P., Craig, T., Dupont, F., DuVivier, A., Grumbine, R., Hebert, D., Holland, M., Jeffery, N., Lemieux, J.F., Rasmussen, T., Ribergaard, M., Roberts, A., Turner, M., Winton, M., 2019. CICE-Consortium/Icepack: Icepack1.1.1. Zenodo, http://dx.doi.org/10.5281/ZENODO.3251032, URL https://zenodo.org/record/3251032.

Hunke, Elizabeth C., Hebert, David A., Lecomte, Olivier, 2013. Level-ice melt ponds in the Los Alamos sea ice model, CICE. Ocean Model. 71, 26–42. http://dx.doi.org/10.1016/j.ocemod.2012.11.008.

Kim, Joo-Hong, Moon, Woosok, Wells, Andrew J., Wilkinson, Jeremy P., Langton, Tom, Hwang, Byongjun, Granskog, Mats A., Jones, David W. Rees, 2018. Salinity control of thermal evolution of late summer melt ponds on Arctic sea ice. Geophys. Res. Lett. 45 (16), 8304–8313. http://dx.doi.org/10.1029/2018gl078077, Publisher: American Geophysical Union (AGU).

Kobayashi, Shinya, Ota, Yukinari, Harada, Yayoi, Ebita, Ayataka, Moriya, Masami, Onoda, Hirokatsu, Onogi, Kazutoshi, Kamahori, Hirotaka, Kobayashi, Chiaki, Endo, Hirokazu, Miyaoka, Kengo, Takahashi, Kiyotoshi, 2015. The JRA-55 reanalysis: General specifications and basic characteristics. J. Meteorol. Soc. Jpn. Ser. II 93 (1), 5–48. http://dx.doi.org/10.2151/jmsj.2015-001.

Kwok, R., Rothrock, D.A., 2009. Decline in Arctic sea ice thickness from submarine and icesat records: 1958-2008. Geophys. Res. Lett. 36 (15), n/a–n/a. http://dx.doi.org/10.1029/2009gl039035.

Large, W., Yeager, S., 2004. Diurnal to decadal global forcing for ocean and sea-ice models: The data sets and flux climatologies. Univ. Corp. Atmos. Res. (NCAR/TN-460+STR), http://dx.doi.org/10.5065/D6KK98Q6, URL http://opensky.ucar.edu/islandora/object/technotes:434.

Large, W.G., Yeager, S.G., 2008. The global climatology of an interannually varying air–sea flux data set. Clim. Dynam. 33 (2–3), 341–364. http://dx.doi.org/10.1007/s00382-008-0441-3.

Lecomte, O., Fichefet, T., Flocco, D., Schroeder, D., Vancoppenolle, M., 2015. Interactions between wind-blown snow redistribution and melt ponds in a coupled ocean-sea ice model. Ocean Model. 87, 67–80. http://dx.doi.org/10.1016/j.ocemod.2014.12.003, URL https://www.sciencedirect.com/science/article/pii/S1463500314001784.

Lecomte, O., Fichefet, T., Vancoppenolle, M., Nicolaus, M., 2011. A new snow thermodynamic scheme for large-scale sea-ice models. Ann. Glaciol. 52 (57 PART 2), 337–346. http://dx.doi.org/10.3189/172756411795931453.

Ledley, Tamara Shapiro, 1985. Sensitivity of a thermodynamic sea ice model with leads to time step size. J. Geophys. Res. 90 (D1), 2251. http://dx.doi.org/10.1029/jd090id01p02251.

Lee, S., Stroeve, J., Tsamados, M., Khan, Alia L., 2020. Machine learning approaches to retrieve pan-Arctic melt ponds from visible satellite imagery. Remote Sens. Environ. (ISSN: 0034-4257) 247, 111919. http://dx.doi.org/10.1016/j.rse.2020.111919, URL http://www.sciencedirect.com/science/article/pii/S0034425720302893.

Locarnini, Ricardo A., Mishonov, Alexey V., Antonov, John I., Boyer, Timothy P., Garcia, Hernan E., Baranova, Olga K., Zweng, Melissa M., Paver, Christopher R., Reagan, James R., Johnson, Daphne R., Hamilton, Melanie, Seidov, Dan, 1948, Levitus, Sydney, 2013. World ocean atlas 2013. volume 1, temperature. http://dx.doi.org/10.7289/V55X26VD, URL https://repository.library.noaa.gov/view/noaa/14847.

Lüpkes, C., Gryanik, V.M., Rösel, A., Birnbaum, G., Kaleschke, L., 2013. Effect of sea ice morphology during Arctic summer on atmospheric drag coefficients used in climate models. Geophys. Res. Lett. 40 (2), 446–451.

Lüthje, Mikael, Feltham, D.L., Taylor, P.D., Worster, M. Grae, 2006. Modeling the summertime evolution of sea-ice melt ponds. J. Geophys. Res. Oceans (ISSN: 21699291) 111 (2), C02001. http://dx.doi.org/10.1029/2004JC002818.

Madec, Gurvan, Bourdallé-Badie, Romain, Bouttier, Pierre-Antoine, Bricaud, Clément, Bruciaferri, Diego, Calvert, Daley, Chanut, Jérôme, Clementi, Emanuela, Coward, Andrew, Delrosso, Damiano, Ethé, Christian, Flavoni, Simona, Graham, Tim, Harle, James, Iovino, Doroteaciro, Lea, Dan, Lévy, Claire, Lovato, Tomas, Martin, Nicolas, Masson, Sébastien, Mocavero, Silvia, Paul, Julien, Rousset, Clément, Storkey, Dave, Storto, Andrea, Vancoppenolle, Martin, 2017. NEMO ocean engine. Zenodo, http://dx.doi.org/10.5281/zenodo.3248739.

Madec, Gurvan, Imbard, Maurice, 1996. A global ocean mesh to overcome the north pole singularity. Clim. Dynam. 12 (6), 381–388. http://dx.doi.org/10.1007/bf00211684.

Maslanik, James, Stroeve, Julienne, Fowler, Charles, Emery, William, 2011. Distribution and trends in Arctic sea ice age through spring 2011. Geophys. Res. Lett. 38 (13), n/a–n/a. http://dx.doi.org/10.1029/2011gl047735.

Massonnet, François, Barthélemy, Antoine, Worou, Koffi, Fichefet, Thierry, Vancoppenolle, Martin, Rousset, Clément, Moreno-Chamarro, Eduardo, 2019. On the discretization of the ice thickness distribution in the NEMO3.6-LIM3 global ocean–sea ice model. Geosci. Model Dev. 12 (8), 3745–3758. http://dx.doi.org/10.5194/gmd-12-3745-2019, Publisher: Copernicus GmbH.

Merino, Nacho, Sommer, Julien Le, Durand, Gael, Jourdain, Nicolas C., Madec, Gurvan, Mathiot, Pierre, Tournadre, Jean, 2016. Antarctic icebergs melt over the southern ocean: Climatology and impact on sea ice. Ocean Model. 104, 99–110. http://dx.doi.org/10.1016/j.ocemod.2016.05.001.

Morassutti, M.P., Ledrew, B.F., 1996. Albedo and depth of melt ponds on sea-ice. Int. J. Climatol. (ISSN: 08998418) 16 (7), 817–838. http://dx.doi.org/10.1002/(SICI)1097-0088(199607)16:7<817::AID-JOC44>3.0.CO;2-5.

Notz, Dirk, 2005. Thermodynamic and Fluid-Dynamical Processes in Sea Ice. (Ph.D. thesis). Institute of Theoretical Geophysics, Department of Applied Mathematics and Theoretical Physics, University of Cambridge, Cambridge.

Oberhuber, Josef M., 1988. An Atlas Based on the 'Coads' Data Set: The Budgets of Heat, Buoyancy and Turbulent Kinetic Energy at the Surface of Global Ocean. Technical Report, (15), Max-Planck-Institute for Meteorology, 2000 hamburg 13, bundesstrasse 55, FRG.

Pedersen, Christina A., Roeckner, Erich, Lüthje, Mikael, Winther, Jan Gunnar, 2009. A new sea ice albedo scheme including melt ponds for ECHAM5 general circulation model. J. Geophys. Res.: Atmos. (ISSN: 01480227) 114 (8), D08101. http://dx.doi.org/10.1029/2008JD010440.

Pegau, W. Scott, Paulson, Clayton A., 2001. The albedo of Arctic leads in summer. Ann. Glaciol. 33, 221–224. http://dx.doi.org/10.3189/172756401781818833.

Perovich, Donald K., 2003. Thin and thinner: Sea ice mass balance measurements during SHEBA. J. Geophys. Res. 108 (C3), http://dx.doi.org/10.1029/2001jc001079.

Perovich, Donald K., Grenfell, Thomas C., Light, Bonnie, Elder, Bruce C., Harbeck, Jeremy, Polashenski, Christopher, Tucker, Walter B., Stelmach, Casey, 2009. Transpolar observations of the morphological properties of Arctic sea ice. J. Geophys. Res. 114, http://dx.doi.org/10.1029/2008jc004892, Publisher: American Geophysical Union (AGU).

Perovich, D.K., Jones, K.F., Light, B., Eicken, H., Markus, T., Stroeve, J., Lindsay, R., 2011. Solar partitioning in a changing Arctic sea-ice cover. Ann. Glaciol. 52 (57), 192–196. http://dx.doi.org/10.3189/172756411795931543.

Polashenski, Chris, Perovich, Donald, Courville, Zoe, 2012. The mechanisms of sea ice melt pond formation and evolution. J. Geophys. Res. Oceans (ISSN: 21699291) 117 (1), http://dx.doi.org/10.1029/2011JC007231.

Prather, Michael J., 1986. Numerical advection by conservation of second-order moments. J. Geophys. Res. 91 (D6), 6671. http://dx.doi.org/10.1029/jd091id06p06671.

Riihelä, Aku, Manninen, Terhikki, Laine, Vesa, 2013. Observed changes in the albedo of the Arctic sea-ice zone for the period 1982–2009. Nature Clim. Change 3 (10), 895–898. http://dx.doi.org/10.1038/nclimate1963.

Rösel, A., Kaleschke, L., Birnbaum, G., 2012. Melt ponds on Arctic sea ice determined from MODIS satellite data using an artificial neural network. Cryosphere 6 (2), 431–446. http://dx.doi.org/10.5194/tc-6-431-2012.

Rousset, C., Vancoppenolle, M., Madec, G., Fichefet, T., Flavoni, S., Barthélemy, A., Benshila, R., Chanut, J., Levy, C., Masson, S., Vivier, F., 2015. The Louvain-La-Neuve sea ice model LIM3.6: global and regional capabilities. Geosci. Model Dev. 8 (10), 2991–3005. http://dx.doi.org/10.5194/gmd-8-2991-2015.

Schröder, D., Feltham, D.L., Flocco, D., Tsamados, M., 2014. September Arctic sea-ice minimum predicted by spring melt-pond fraction. Nature Clim. Change 4, 353. http://dx.doi.org/10.1038/nclimate2203.

Schweiger, Axel, Lindsay, Ron, Zhang, Jinlun, Steele, Mike, Stern, Harry, Kwok, Ron, 2011. Uncertainty in modeled Arctic sea ice volume. J. Geophys. Res. 116, http://dx.doi.org/10.1029/2011jc007084.

Scott, F., Feltham, D.L., 2010. A model of the three-dimensional evolution of Arctic melt ponds on first-year and multiyear sea ice. J. Geophys. Res. Oceans 115 (12), C12064. http://dx.doi.org/10.1029/2010JC006156.

Serreze, Mark C., Meier, Walter N., 2018. The Arctic's sea ice cover: trends, variability, predictability, and comparisons to the Antarctic. Ann. New York Acad. Sci. 1436 (1), 36–53. http://dx.doi.org/10.1111/nyas.13856.

Shine, K.P., Henderson-Sellers, A., 1985. The sensitivity of a thermodynamic sea ice model to changes in surface albedo parameterization. J. Geophys. Res. 90 (D1), 2243. http://dx.doi.org/10.1029/jd090id01p02243.

Thorndike, A.S., Rothrock, D.A., Maykut, G.A., Colony, R., 1975. The thickness distribution of sea ice. J. Geophys. Res. 80 (33), 4501–4513. http://dx.doi.org/10.1029/jc080i033p04501.

Tsamados, M., Feltham, D.L., Schroeder, D., Flocco, D., Farrell, S.L., Kurtz, N., Laxon, S.W., Bacon, S., 2014. Impact of variable atmospheric and oceanic form drag on simulations of Arctic sea ice. J. Phys. Oceanogr. 44 (5), 1329–1353. http://dx.doi.org/10.1175/jpo-d-13-0215.1.

Tschudi, M., Maslanik, J.A., Perovich, D.K., 2005. Melt pond coverage on Arctic sea ice from modis. In: 85th AMS Annual Meeting, American Meteorological Society - Combined Preprints. pp. 4067–4070.

Tschudi, Mark A., Maslanik, James A., Perovich, Donald K., 2008. Derivation of melt pond coverage on Arctic sea ice using MODIS observations. Remote Sens. Environ. 112 (5), 2605–2614. http://dx.doi.org/10.1016/j.rse.2007.12.009.

Turner, Adrian K., Hunke, Elizabeth C., 2015. Impacts of a mushy-layer thermodynamic approach in global sea-ice simulations using the CICE sea-ice model. J. Geophys. Res. Oceans 120 (2), 1253–1275. http://dx.doi.org/10.1002/2014jc010358, Publisher: American Geophysical Union (AGU).

Uppala, S.M., KÅllberg, P.W., Simmons, A.J., Andrae, U., Bechtold, V. Da Costa, Fiorino, M., Gibson, J.K., Haseler, J., Hernandez, A., Kelly, G.A., Li, X., Onogi, K., Saarinen, S., Sokka, N., Allan, R.P., Andersson, E., Arpe, K., Balmaseda, M.A., Beljaars, A.C.M., Berg, L. Van De, Bidlot, J., Bormann, N., Caires, S., Chevallier, F., Dethof, A., Dragosavac, M., Fisher, M., Fuentes, M., Hagemann, S., Hólm, E., Hoskins, B.J., Isaksen, L., Janssen, P.A.E.M, Jenne, R., Mcnally, A.P., Mahfouf, J.-F., Morcrette, J.-J., Rayner, N.A., Saunders, R.W., Simon, P., Sterl, A., Trenberth, K.E., Untch, A., Vasiljevic, D., Viterbo, P., Woollen, J., 2005. The ERA-40 re-analysis. Q. J. R. Meteorol. Soc. 131 (612), 2961–3012. http://dx.doi.org/10.1256/qj.04.176.

Vancoppenolle, Martin, Bitz, Cecilia M., Fichefet, Thierry, 2007. Summer landfast sea ice desalination at point Barrow, Alaska: Modeling and observations. J. Geophys. Res. 112 (C4), http://dx.doi.org/10.1029/2006jc003493,

Vancoppenolle, Martin, Fichefet, Thierry, Goosse, Hugues, Bouillon, Sylvain, Madec, Gurvan, Maqueda, Miguel Angel Morales, 2009. Simulating the mass balance and salinity of Arctic and Antarctic sea ice. 1. Model description and validation. Ocean Model. 27 (1–2), 33–53. http://dx.doi.org/10.1016/j.ocemod.2008.10.005.

Webster, Melinda A., Rigor, Ignatius G., Perovich, Donald K., Richter-Menge, Jacqueline A., Polashenski, Christopher M., Light, Bonnie, 2015. Seasonal evolution of melt ponds on Arctic sea ice. J. Geophys. Res. Oceans (ISSN: 21699291) 120 (9), 5968–5982. http://dx.doi.org/10.1002/2015JC011030.

Zhang, Jinlun, Schweiger, Axel, Webster, Melinda, Light, Bonnie, Steele, Michael, Ashjian, Carin, Campbell, Robert, Spitz, Yvette, 2018. Melt pond conditions on declining Arctic sea ice over 1979-2016: Model development, validation, and results. J. Geophys. Res. Oceans 123 (11), 7983–8003. http://dx.doi.org/10.1029/2018jc014298.

Zweng, Melissa M., Reagan, James R., Antonov, John I., Locarnini, Ricardo A., Mishonov, Alexey V., Boyer, Timothy P., Garcia, Hernan E., Baranova, Olga K., Johnson, Daphne R., Seidov, Dan, 1948, Biddle, Mathew M., Levitus, Sydney, 2013. World ocean atlas 2013. volume 2, salinity. http://dx.doi.org/10.7289/V5251G4D, URL https://repository.library.noaa.gov/view/noaa/14848.